

# Non-smooth dynamics of buckling based metainterfaces: rocking-like motion and bifurcations

N. HIMA<sup>1,2</sup>, F. D'ANNIBALE<sup>3,4</sup> AND F. DAL CORSO<sup>\*1</sup>

<sup>1</sup>*DICAM, University of Trento, via Mesiano 77, I-38123 Trento, Italy*

<sup>2</sup>*FIP MEC srl, via Scapacchiò 41, 35030 Selvazzano Dentro PD, Italy*

<sup>3</sup>*DICEAA, University of L'Aquila, L'Aquila, Italy*

<sup>4</sup>*M&MOCS, University of L'Aquila, L'Aquila, Italy*

December 13, 2022

## Abstract

The non-smooth dynamics is investigated for an elastic planar metainterface composed by two layers of buckling elements, each one allowing motion on one side only. Through the analogy between buckling and unilateral contact and by assuming no-bouncing at impact, the motion of the relevant two degrees of freedom system is reduced to that of a single degree governed by a piecewise-smooth differential equation. The metainterface dynamics has strong similarities with the rocking motion of rigid blocks and displays several types of dynamic bifurcations in the presence of oscillatory forces, including period doubling, branch point cycle, grazing, as well as quasi-periodic and chaotic responses. Moreover, the multistable response is found to be broaden to conditions representative of monostable states within a quasi-static setting, disclosing a multistability anticipation by dynamics. The wide landscape of the dynamic response for the buckling based metainterface provides a novel theoretical framework to be exploited in the design of mechanical devices for vibration attenuation and for energy harvesting.

**Keywords:** Nonlinear dynamics, period doubling, grazing, multistability anticipation.

## 1 Introduction

Mechanical instability, a classical scientific field initiated around a quarter of millennium ago by Euler, is nowadays living a second youth. Beside the traditional design principles relied on the rule to avoid instabilities, a new paradigm emerged over the last decades: to exploit instabilities for attaining novel and desired features [1]. This new design perspective is being explored in many technological sectors, encompassing high-damping and energy-absorbing systems [2, 3, 4, 5], wave guiding and manipulation [6, 7, 8], deployable structures [9, 10, 11] and locomotion [12, 13]. Towards a further advancement in these sectors, several intriguing findings have been recently discovered in the realm of structural stability as, for example among the many, the buckling under tensile load [14, 15], the restabilization of the trivial path for one-dimensional [16, 17, 18] and bi-dimensional [19, 20, 21] structures, the flutter instability of conservative systems triggered by non-holonomic constraints [22, 23], the snapping, coiling, and folding of structures through interaction with fluids [24, 25, 26], and instability-driven morphologies [27, 28, 29].

The modeling and design of meta-structures and meta-interfaces is a challenging task for scholars and researchers in mechanics towards the achievement of a designed, tuned, response from a structure or a material (the reader is referred to [30, 31, 32] for mechanical metamaterials, metadevices, and microsystems integration

---

\*Corresponding author: francesco.dalcorso@unitn.it

in metamaterials). Interesting phenomena such as complex nonlinear dynamics, bifurcations, chaotic motions may arise and need for an in-depth analytical, numerical and experimental investigation, as the behaviour of many mechanical systems relies on the large amplitude motion of their components. For example, concepts from dynamical system theory are applied to build up a framework for designing fully nonlinear motions of lattice mechanical materials [33]. Complex dynamics can also take place in nonlinear piezoelectric mechanical systems, where linear and nonlinear damping together with piezoelectric coupling may entail some challenging issues in passive control of flutter instability and post-critical behaviour [34, 35]. Moreover, stress and strain distributions may be controlled through active mechanical metamaterials, as for example by means of piezostack actuators and compliant mechanisms, interconnected to an active metamaterial lattice [36]. Advanced dynamic performances can be also attained through specific periodic microstructures realized with, among different topologies, one-dimensional cellular lattices build up by a pantograph mechanism in the tetra-atomic cell and behaving as an inertially amplified metamaterial [37].

Within this context, the mechanical response of an elastic metainterface (Fig. 1-a) based on two layers of buckling elements is investigated. The unit structural cell of this interface (Fig. 1-b) is composed by stiff bars joined together through hinges and it can be deformed by storing the elastic energy in two rotational springs and by means of the slider presence along two diagonal bars. In particular, the slider enables the bifurcation of the relevant bar at null tensile axial force, which in turn may be exploited to realize a desired mechanical behaviour. The quasi-static behaviour of this unit element has been analyzed in [38] by showing (i.) the equivalence of the tensile (or compressive) buckling element with a unilateral constraint and (ii.) the possibility to realize a multistable device with tunable mechanical response, despite the corresponding small number of degrees of freedom.

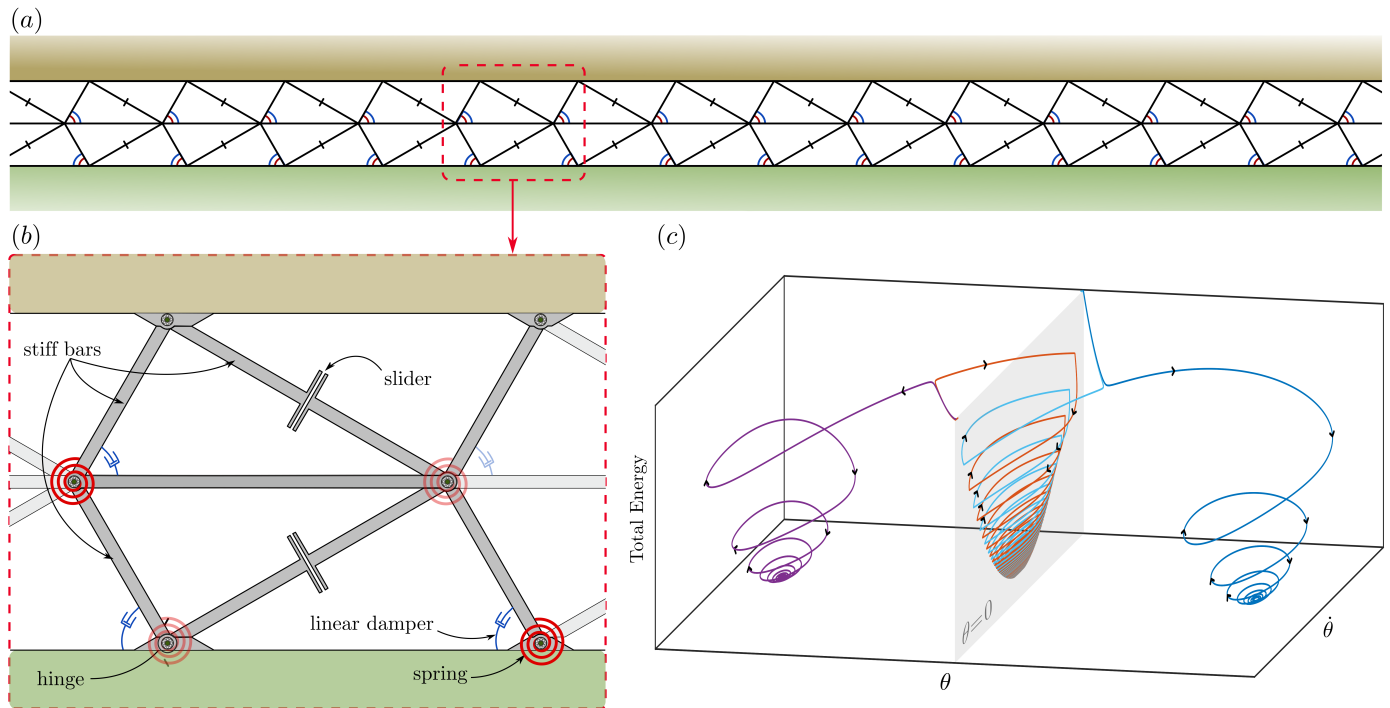


Figure 1: (a) The metainterface based on two layers of tensile-buckling elements and displaying a piecewise-smooth dynamics. (b) The unit structural cell composed by stiff bars, rotational springs, dampers and sliders. (c) Vibrations trajectories for a nonconservative tristable metainterface under constant symmetric loading conditions (dataset of Fig. 4-c) within the rotation-angular velocity-total energy space, together with the system discontinuity plane (grey) corresponding to the undeformed configuration.

The objective of the present research is to extend the mechanical behaviour analysis of the unit cell to

dynamic conditions. The kinematics of this system is dependent on two degree of freedom system (Sect. 2) and the motion is governed by two coupled nonlinear ordinary differential equations subject to unilateral constraints (Sect. 3). Such constraints limit each layer of the structure to a unilateral motion, which in turn leads to various impact scenarios, differing in the bouncing, no-bouncing, or partial-bouncing of the impacting layer (Sect. 4). Under the assumption of no bouncing occurrence, the motion analysis reduces to that of a single degree of freedom described by a piecewise-smooth differential equation [39, 40, 41], with the switching plane corresponding to the undeformed equilibrium configuration (Fig. 1-c). The non-smoothness in the response is always realized through an acceleration jump and, depending on impact dissipation phenomena, also through a possible velocity jump.

Vibration analysis under constant symmetric loading reveals strong similarities with the classical rocking motion of rectangular rigid bodies in rigid surfaces (Sect. 5), mainly differing for the absence of the first order term of the rotations due to rotational spring in the present system. Small amplitude vibration analysis sheds light over the finite time decay of the free rocking-like motion (Sect. 5.1). Phase portraits at large amplitude vibrations disclose the influence of different damping mechanisms and system non-symmetry on the motion, showing the possible existence of three stable attractors within a feasible range of deformations (Sect. 5.2). Moreover, systems with extreme stiffness ratios display an intriguing bouncing-like behaviour even under no bouncing assumption (Sect. 5.3).

Response spectra and bifurcation diagrams reveal a rich mechanical behaviour of the system under oscillatory loading conditions, including primary and super-harmonic resonances, period-doubling cascades, quasi-periodic and chaotic behaviour, grazing, and coexistence of stable equilibrium paths within a chaotic region (Sect 6). Finally, depending on the force velocity, the interplay between external and parametric excitation may provide a bistable response at load amplitudes corresponding to a monostable response under the quasi-static assumption. As a consequence, dynamic effects realize a multistability anticipation for the system.

The obtained results show the possibility to harness bifurcation phenomena of the present structural system to display highly desirable mechanical features, without compromising the global stability of the system. Moreover, the multistable and multisource dissipation mechanisms embedded in the considered metainterface concept open new possibilities in the design of technological devices for vibration attenuation and energy harvesting.

## 2 Mechanical model for the structural unit cell

The mechanical response is addressed for a planar structural system made up of two layers of an articulated quadrilateral structure with parallelogram shape, realized by rigid bars connected to one another through hinges and with dimension scaled through the length  $l$ , corresponding to that of the inclined bars along the parallelogram perimeter (Fig. 2). Two visco-elastic hinges are present by adding linear rotational springs of stiffness  $K_1$  and  $K_2$ , and dashpots of viscous coefficients  $C_1$  and  $C_2$  respectively to the hinges located at the points ‘A’ and ‘B’, while two sliders are located at the mid-span of a diagonal of each parallelogram. Since each slider constraints the continuity in axial and rotational displacements but allows for a jump in the transverse displacement, the  $j$ -th layer may deform into another parallelogram described by the configuration angles  $\alpha_j$  and  $\beta_j$ , which are functions of the misalignment angle  $\varphi_j$  displayed at the relevant slider as

$$\alpha_j(\varphi_j) = \arccos\left(\frac{\psi}{2\lambda \cos \varphi_j} + \chi \cos \varphi_j\right), \quad \beta_j(\varphi_j) = \arccos(\cos \beta_0 - \psi \tan^2 \varphi_j) \geq \beta_0, \quad (1)$$

where  $\psi$ ,  $\lambda$  and  $\chi$  are constants defined as

$$\psi = \frac{\sin \beta_0^2}{2 \sin \alpha_0 \sin(\alpha_0 + \beta_0)}, \quad \lambda = \frac{\sin \beta_0}{2 \sin \alpha_0} > 0, \quad \chi = \frac{\sin(2\alpha_0 + \beta_0)}{\sin(\alpha_0 + \beta_0)}, \quad (2)$$

being  $\alpha_0$  and  $\beta_0$  the angles describing the undeformed configuration,  $\alpha_j(\phi_j = 0) = \alpha_0$  and  $\beta_j(\phi_j = 0) = \beta_0$ , and subject to the following constraints

$$\alpha_0 > 0, \quad 0 < \beta_0 < \pi, \quad \alpha_0 + \beta_0 < \pi. \quad (3)$$

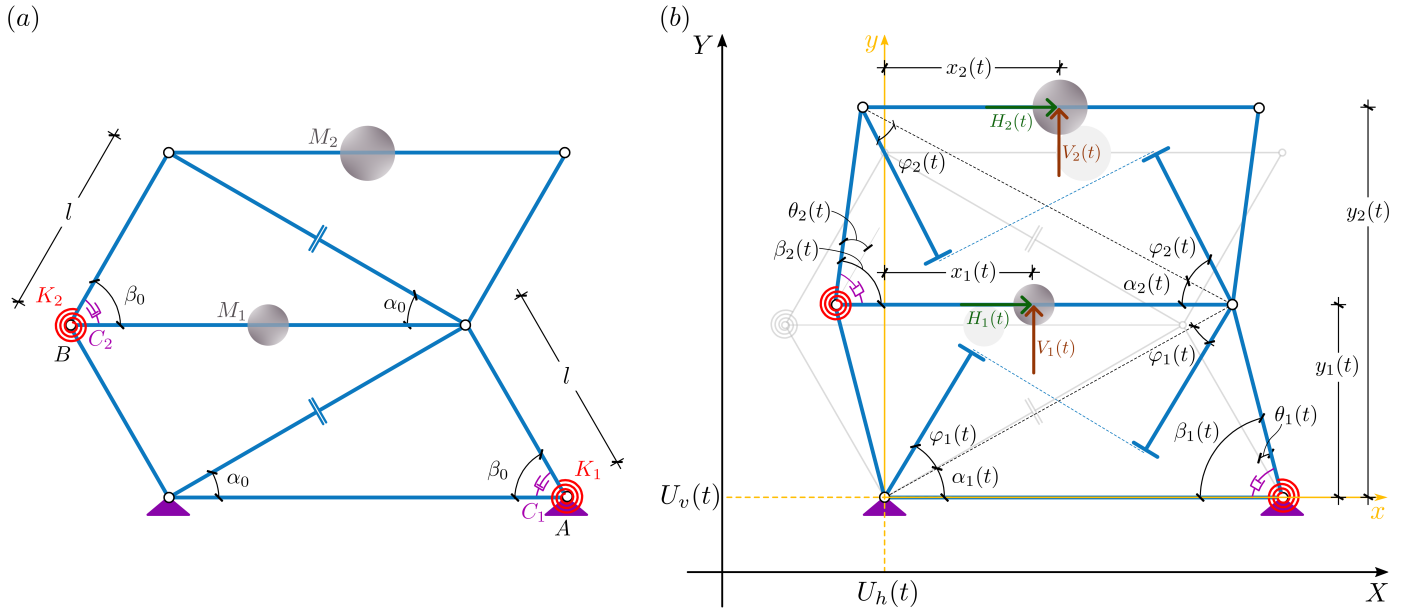


Figure 2: (a) Undeformed and (b) deformed configuration for the unit structural cell composing the metainterface in Fig. 1. The unit cell is made up of two articulated quadrilateral structures, each one composed of rigid bars and containing a visco-elastic hinge (of stiffness  $K_j$  and viscous coefficient  $C_j$ ,  $j = 1, 2$ ) and a slider at the midpoint of the diagonal bar within the parallelogram. Loading is applied by means of horizontal  $H_j(t)$  and vertical  $V_j(t)$  forces at the  $j$ -th layer and of ground horizontal  $U_h(t)$  and vertical  $U_v(t)$  displacements. The deformed configuration can be described through the misalignment angles  $\varphi_j$  or through the difference angles  $\theta_j$ , where the latter measure is the most appropriate to investigate the dynamic response.

The inertia of the system is modelled through the mass  $M_j$  attached to the central point along the top edge of the  $j$ -th layer. Because the motion of the top edge of each layer is described by a rigid translation without any rotation, the possible presence of rotational inertia has no effect in the present analysis. The position of the mass relevant to the  $j$ -th layer is described with varying of the physical time  $t$  through its absolute coordinates  $X_j(t)$  and  $Y_j(t)$ , evaluated as

$$\begin{cases} X_j(t) = U_h(t) + x_j(t), \\ Y_j(t) = U_v(t) + y_j(t), \end{cases} \quad (4)$$

where  $x_j(t)$  and  $y_j(t)$  are the relative coordinates of the same point measured in the  $x - y$  non-inertial frame, attached to the lattice base and with origin located at the lower left hinge, while  $U_h(t)$  and  $U_v(t)$  measure the ground motion of the  $x - y$  non-inertial frame with respect to the  $X - Y$  inertial frame.

In order to proceed with a non-dimensional analysis, the dimensionless time  $\tau$  is introduced as

$$\tau = \frac{t}{T}, \quad (5)$$

where the characteristic time  $T$  is considered as

$$T = \sqrt{\frac{M_2 l^2}{K_2}}. \quad (6)$$

Moreover, dimensionless ground motion components are introduced as

$$\zeta(\tau) = \frac{U_h(\tau)}{l}, \quad \nu(\tau) = \frac{U_v(\tau)}{l}, \quad (7)$$



as well as the following relative dimensionless horizontal and vertical coordinates

$$\begin{aligned}\xi_1(\tau) &= \frac{x_1(\tau)}{l} + \frac{\sin(\alpha_0 - \beta_0)}{2 \sin \alpha_0}, & \xi_2(\tau) &= \frac{x_2(\tau) - x_1(\tau)}{l} - \cos \beta_0, \\ \eta_1(\tau) &= \frac{y_1(\tau)}{l}, & \eta_2(\tau) &= \frac{y_2(\tau) - y_1(\tau)}{l}.\end{aligned}\quad (8)$$

Interestingly, the deformed configuration of the  $j$ -th layer can also be described through the difference angle  $\theta_j$  at the respective visco-elastic hinge, defined as a function of the misalignment angle  $\varphi_j$  through

$$\theta_j(\tau) = (-1)^j [\beta_j(\varphi_j(\tau)) - \beta_0], \quad (9)$$

implying the following inequalities

$$\theta_1(\tau) \geq 0, \quad \theta_2(\tau) \leq 0 \quad \Rightarrow \quad \theta_1(\tau)\theta_2(\tau) \leq 0. \quad (10)$$

In the quasi-static analysis of the present system [38], it has been shown that the deformed configuration of the layers is realized through a bifurcation of system referred to the misalignment angles  $\varphi_j$  or in the presence of unilateral constraints when the difference angles  $\theta_j$  are considered, because restricted to satisfy eqn. (10). Although in practical terms the two measures of angles are equivalent within a quasi-static setting, the difference angles  $\theta_j(\tau)$  represent the best measure to refer when performing a dynamic analysis. Indeed, the misalignment angle  $\varphi_j$  assumes infinite velocity at the impact of the  $j$ -th layer, namely when it approaches zero, providing difficulties in the convergence of numerical integration of the equation of motions at each impact condition. This is made evident by recalling that the misalignment and the difference angles are related to each other under small rotations through

$$|\theta_j(\tau)| \approx \frac{\psi}{\sin \beta_0} \varphi_j^2(\tau), \quad \text{for} \quad |\varphi_j| \rightarrow 0, \quad (11)$$

and evaluating its derivative,

$$|\dot{\theta}_j(\tau)| \approx \frac{2\psi}{\sin \beta_0} |\varphi_j(\tau)| |\dot{\varphi}_j(\tau)|, \quad (12)$$

the singular behaviour of the misalignment angle velocity  $\dot{\varphi}_j(\tau^*)$  at the impact time  $\tau^*$  (defining  $\varphi_j(\tau^*) = 0$ ) is implied by assuming a corresponding finite magnitude of the difference angle velocity  $|\dot{\theta}_j(\tau^*)|$ . This behaviour is graphically represented in Fig. 3 through *a*) the generic evolution in time of the angle measures and *b*) their phase portraits are reported for time  $\tau$  close to that of impact  $\tau^*$ .

Due to the above-mentioned motivation, it is instrumental to express the kinematic parameters  $\xi_j$ , and  $\eta_j$  to the respective difference angle  $\theta_j$  through the following expressions <sup>1</sup>

$$\xi_j(\tau) = -(-1)^j (\cos \beta_0 - \cos (\beta_0 - (-1)^j \theta_j(\tau))), \quad \eta_j(\tau) = \sin (\beta_0 - (-1)^j \theta_j(\tau)). \quad (14)$$

Finally, it is noted that the  $j$ -th parallelogram reduces into a line segment when the difference angle takes the following special values

$$|\theta_j| = \bar{\theta}^{[n]}, \quad \text{where} \quad \bar{\theta}^{[n]} = n\pi - \beta_0, \quad n \in \mathbb{N}. \quad (15)$$

<sup>1</sup>For completeness, the configuration angle  $\alpha_j$  as a function of the difference angle  $\theta_j$  is given by

$$\alpha_j(\tau) = \operatorname{arcsec} \left[ \sqrt{\frac{\cos \beta_0 - \cos (\beta_0 + (-1)^j \theta_j(\tau)) + \psi}{\psi}} \frac{2\lambda}{\cos \beta_0 - \cos (\beta_0 + (-1)^j \theta_j(\tau)) + 2\lambda\chi + \psi} \right]. \quad (13)$$

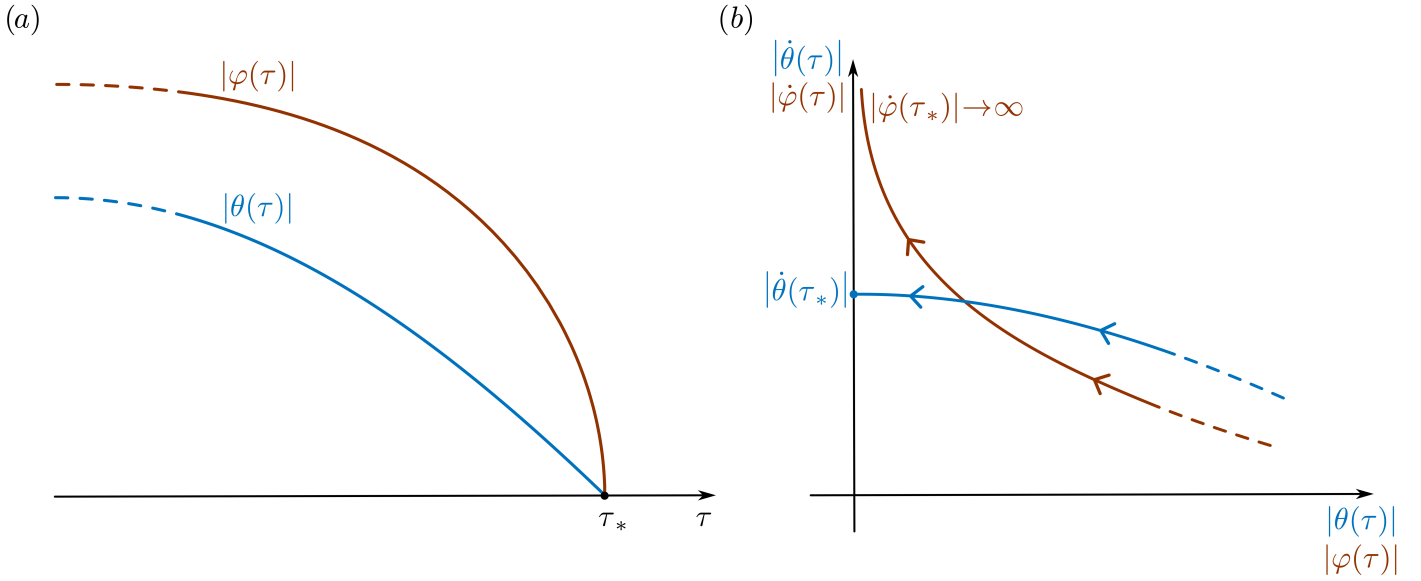


Figure 3: Schematic representation of (a) the evolution in the dimensionless time  $\tau$  and of (b) the phase portraits for the modulus of the misalignment angle  $|\varphi|$  and of the difference angle  $|\theta|$  just before the impact time  $\tau_*$ . A singular value for the velocity of the misalignment angle is displayed at the impact,  $|\dot{\varphi}(\tau_*)| \rightarrow \infty$ , therefore the dynamic analysis of the structural system has to be performed with reference to the difference angle  $\theta(\tau)$  in order to overcome numerical integration issues.

The above condition evaluated at  $n = 1$  may represent a limitation to the motion of the system if impact between the different rigid bars occurs. However, if the related dimension of connected object allows, this situation can be circumvented by realizing the structural system exploiting the out-of-plane direction. Indeed, when the rigid bars are located on different planes, their rotations can monotonically increase in magnitude without any limitation except for the energy that can be possibly stored within the respective rotational spring. In any case, independently of this aspect, eqn. (15) defines an upper bound to the magnitude of the relative horizontal displacement  $\xi_j$  that can be displayed by the mass  $M_j$

$$|\xi_j| < \bar{\xi}, \quad \text{where} \quad \bar{\xi} = 1 + \cos \beta_0. \quad (16)$$

### 3 The Lagrangian and the equations of motion

The kinetic energy  $\mathcal{T}$  of the system under consideration (Fig. 2) can be expressed as a function of the difference angles  $\theta_j$  and their velocities  $\dot{\theta}_j$  ( $j = 1, 2$ ) as

$$\mathcal{T} = \frac{K_2}{2} \sum_{j=1}^2 [(2-j)m + j - 1] \left\{ \left[ \dot{\zeta}(\tau) + (j-1) \sin(\beta_0 + \theta_1(\tau)) \dot{\theta}_1(\tau) + \sin(\beta_0 - (-1)^j \theta_j(\tau)) \dot{\theta}_j(\tau) \right]^2 + \left[ \dot{\nu}(\tau) + (j-1) \cos(\beta_0 + \theta_1(\tau)) \dot{\theta}_1(\tau) - (-1)^j \cos(\beta_0 - (-1)^j \theta_j(\tau)) \dot{\theta}_j(\tau) \right]^2 \right\}, \quad (17)$$

while its potential energy  $\Pi$  is given as the sum of the elastic energy stored in the two rotational springs as follows

$$\Pi = \frac{K_2}{2} \sum_{j=1}^2 [(2-j)k + j - 1] \theta_j(\tau)^2, \quad (18)$$

with the mass ratio  $m$  and the stiffness ratio  $k$  introduced as

$$m = \frac{M_1}{M_2}, \quad k = \frac{K_1}{K_2}. \quad (19)$$

The presence of the viscous dampers (with damping coefficient  $C_j$ ) at the hinges located at points ‘A’ and ‘B’ (Fig. 2), to account for the possible air resistance and other sources of dissipation during the motion, leads to the following Rayleigh dissipation function  $\mathcal{R}$

$$\mathcal{R} = K_2 \frac{\mathcal{C}}{2} \sum_{j=1}^2 [(2-j)c + j-1] \dot{\theta}_j(\tau)^2, \quad (20)$$

where the dissipation ratio  $c$  and the damping ratio  $\mathcal{C}$  are introduced as

$$c = \frac{C_1}{C_2}, \quad \mathcal{C} = \frac{C_2}{M_2 l^2}. \quad (21)$$

By considering the Lagrangian  $\mathcal{L} = \mathcal{T} - \Pi$  and the Rayleigh dissipation function  $\mathcal{R}$ , the equations of motion can be obtained through the Euler-Lagrange equation,

$$\frac{d}{d\tau} \left( \frac{\partial \mathcal{L}(\dot{\theta}_1, \dot{\theta}_2, \theta_1, \theta_2)}{\partial \dot{\theta}_j} \right) - \frac{\partial \mathcal{L}(\dot{\theta}_1, \dot{\theta}_2, \theta_1, \theta_2)}{\partial \theta_j} + \frac{\partial \mathcal{R}(\dot{\theta}_1, \dot{\theta}_2)}{\partial \dot{\theta}_j} = \mathcal{Q}_{\theta_j}(\tau), \quad j = 1, 2, \quad (22)$$

where  $\mathcal{Q}_{\theta_j}(\tau)$  is the generalized external forces evaluated through the principle of the virtual work for a virtual rotation  $\delta\theta_j$ . By assuming the set of horizontal  $H_1(t)$ ,  $H_2(t)$  and vertical  $V_1(t)$ ,  $V_2(t)$  forces acting on the masses  $M_1$  and  $M_2$  (as sketched in Fig. 2), the generalized forces  $\mathcal{Q}_{\theta_j}(\tau)$  are evaluated as

$$\begin{aligned} \mathcal{Q}_{\theta_j}(\tau) = & K_2 \left[ (1 + h(\tau))^{2-j} \mathcal{H}(\tau) \sin(\beta_0 - (-1)^j \theta_j(\tau)) \right. \\ & \left. - (-1)^j (1 + v(\tau))^{2-j} \mathcal{V}(\tau) \cos(\beta_0 - (-1)^j \theta_j(\tau)) \right], \quad j = 1, 2, \end{aligned} \quad (23)$$

where the dimensionless external horizontal  $\mathcal{H}(\tau)$  and vertical  $\mathcal{V}(\tau)$  forces and their respective ratios,  $h(\tau)$  and  $v(\tau)$ , have been introduced as

$$\mathcal{H}(\tau) = \frac{H_2(\tau)l}{K_2}, \quad \mathcal{V}(\tau) = \frac{V(\tau)l}{K_2}, \quad h(\tau) = \frac{H_1(\tau)}{H_2(\tau)}, \quad v(\tau) = \frac{V_1(\tau)}{V_2(\tau)}. \quad (24)$$

The equations of motion are then given by the following system of two coupled nonlinear ordinary differential equations for the difference angles  $\theta_j(\tau)$ , restricted by the inequalities (10),

$$\begin{aligned} \mathbf{M}(\theta_1(\tau), \theta_2(\tau)) \begin{Bmatrix} \ddot{\theta}_1(\tau) \\ \ddot{\theta}_2(\tau) \end{Bmatrix} + \mathbf{C} \begin{Bmatrix} \dot{\theta}_1(\tau) \\ \dot{\theta}_2(\tau) \end{Bmatrix} + \mathbf{D}(\theta_1(\tau), \theta_2(\tau)) \begin{Bmatrix} \dot{\theta}_1^2(\tau) \\ \dot{\theta}_2^2(\tau) \end{Bmatrix} \\ + \mathbf{K}(\theta_1(\tau), \theta_2(\tau)) \begin{Bmatrix} \theta_1(\tau) \\ \theta_2(\tau) \end{Bmatrix} = \mathbf{f}(\theta_1(\tau), \theta_2(\tau)), \end{aligned} \quad (25)$$

where  $\mathbf{M}$  is the (symmetric) mass operator,  $\mathbf{C}$  is the diagonal viscous damping matrix,  $\mathbf{D}$  is the (skew-symmetric) operator multiplying the squared angular velocities (springing from kinetic nonlinearities),  $\mathbf{K}$  is

the diagonal stiffness operator, and  $\mathbf{f}$  is the equivalent force vector, defined as

$$\begin{aligned} \mathbf{M} &= \begin{bmatrix} m+1 & -\cos(2\beta_0 + \theta_1(\tau) - \theta_2(\tau)) \\ -\cos(2\beta_0 + \theta_1(\tau) - \theta_2(\tau)) & 1 \end{bmatrix}, & \mathbf{C} &= \mathcal{C} \begin{bmatrix} c & 0 \\ 0 & 1 \end{bmatrix}, \\ \mathbf{D} &= \begin{bmatrix} 0 & -\sin(2\beta_0 + \theta_1(\tau) - \theta_2(\tau)) \\ \sin(2\beta_0 + \theta_1(\tau) - \theta_2(\tau)) & 0 \end{bmatrix}, & \mathbf{K} &= \begin{bmatrix} k & 0 \\ 0 & 1 \end{bmatrix}, \\ \mathbf{f} &= \begin{Bmatrix} [(1+h(\tau))\mathcal{H}(\tau) - (m+1)\ddot{\zeta}(\tau)]\sin(\beta_0 + \theta_1(\tau)) + [(1+v(\tau))\mathcal{V}(\tau) - (m+1)\ddot{v}(\tau)]\cos(\beta_0 + \theta_1(\tau)) \\ [\mathcal{H}(\tau) - \ddot{\zeta}(\tau)]\sin(\beta_0 - \theta_2(\tau)) - [\mathcal{V}(\tau) - \ddot{v}(\tau)]\cos(\beta_0 - \theta_2(\tau)) \end{Bmatrix}. \end{aligned} \quad (26)$$

Under the assumption of oscillations with small amplitudes  $\theta_j(\tau)$ , the equations of motion (25) can be rewritten as the first order truncation of Taylor series as

$$\mathbf{M}_0 \begin{Bmatrix} \ddot{\theta}_1(\tau) \\ \ddot{\theta}_2(\tau) \end{Bmatrix} + \mathbf{C} \begin{Bmatrix} \dot{\theta}_1(\tau) \\ \dot{\theta}_2(\tau) \end{Bmatrix} + \mathbf{K}_0(\tau) \begin{Bmatrix} \theta_1(\tau) \\ \theta_2(\tau) \end{Bmatrix} = \mathbf{f}_0(\tau), \quad (27)$$

where

$$\begin{aligned} \mathbf{M}_0 &= \begin{bmatrix} m+1 & -\cos 2\beta_0 \\ -\cos 2\beta_0 & 1 \end{bmatrix}, & \mathbf{K}_0 &= \begin{bmatrix} \kappa_1(\tau) & 0 \\ 0 & \kappa_2(\tau) \end{bmatrix}, \\ \mathbf{f}_0 &= \begin{Bmatrix} \sin \beta_0 [(h(\tau)+1)\mathcal{H}(\tau) - (m+1)\ddot{\zeta}(\tau)] + \cos \beta_0 [(v(\tau)+1)\mathcal{V}(\tau) - (m+1)\ddot{v}(\tau)] \\ \sin \beta_0 [\mathcal{H}(\tau) - \ddot{\zeta}(\tau)] - \cos \beta_0 [\mathcal{V}(\tau) - \ddot{v}(\tau)] \end{Bmatrix}, \end{aligned} \quad (28)$$

with

$$\begin{aligned} \kappa_j(\tau) &= k^{2-j} + (-1)^j \cos \beta_0 [(h(\tau)+1)^{2-j}\mathcal{H}(\tau) - (m+1)^{2-j}\ddot{\zeta}(\tau)] \\ &\quad + \sin \beta_0 [(v(\tau)+1)^{2-j}\mathcal{V}(\tau) - (m+1)^{2-j}\ddot{v}(\tau)]. \end{aligned} \quad (29)$$

It is noted that both the equivalent force vector  $\mathbf{f}_0$  and the stiffness operator<sup>2</sup>  $\mathbf{K}_0$  have non-constant coefficients whenever the external forces or the ground accelerations vary in time, providing a simultaneous external and parametric excitation to the system.

The obtained equations of motion are complemented in the next Section by the analysis of the possible impact scenarios introduced by the unilateral constraints (10) on the difference angles  $\theta_j(\tau)$ .

#### 4 Impact scenarios, no bouncing assumption, and reduction to a single degree of freedom

During the motion, the deformed  $s$ -th layer of the planar structure may return to its undeformed configuration at the time  $\tau_*$ ,  $\theta_s(\tau_*) = 0$ . Because the  $s$ -th layer can not smoothly continue its motion at  $\tau_*$  due to the unilateral constraint on the difference angle  $\theta_s$ , eqn. (10), an impact occurs realizing an impulse to the structure. The effect of such an impulse is modelled as a non-smooth (instantaneous) transition expressed by a possible jump<sup>3</sup>

<sup>2</sup>It is noted that, for simplicity in nomenclature,  $\mathbf{K}_0$  is defined as the difference of the expansion of  $\mathbf{K}$  and the coefficients of the linear terms in  $\theta_j$  of the expansion of  $\mathbf{f}$ .

<sup>3</sup>In the following, the brackets  $[\![\cdot]\!]$  indicate the jump in the corresponding quantity (velocity or acceleration) at the impact moment  $\tau_*$  and is defined as the difference of that quantity after and before the impact

$$[\![g(\tau_*)]\!] = g(\tau_*^+) - g(\tau_*^-). \quad (30)$$

in the layers velocities at the impact time  $\tau_*$ , while the rotations are continuous

$$\theta_n(\tau_*^-) = \theta_n(\tau_*^+), \quad n = 1, 2. \quad (31)$$

Considering the  $s$ -th layer as the impacting one while the  $j$ -th layer as the other one ( $j \neq s$ ), the possible impact scenarios are listed in Table 1 in terms of the difference angles of the layers just before ( $\tau_*^-$ ) and just after ( $\tau_*^+$ ) the impact. While two cases are possible before the impact (depending on the number of deformed layers), after the impact three conditions can be realized, namely

- *no bouncing*, for which the impacting layer stops and the other one has a velocity jump

$$\dot{\theta}_s(\tau_*^-)\dot{\theta}_s(\tau_*^+) = 0, \quad \dot{\theta}_j(\tau_*^-) \neq \dot{\theta}_j(\tau_*^+), \quad (32)$$

- *bouncing*, for which the impacting layer reverses its motion and the other one has no velocity jump

$$\dot{\theta}_s(\tau_*^-)\dot{\theta}_s(\tau_*^+) < 0, \quad \dot{\theta}_j(\tau_*^-) = \dot{\theta}_j(\tau_*^+), \quad (33)$$

- *partial bouncing*, for which the impacting layer reverses its motion and the other one has a velocity jump

$$\dot{\theta}_s(\tau_*^-)\dot{\theta}_s(\tau_*^+) < 0, \quad \dot{\theta}_j(\tau_*^-) \neq \dot{\theta}_j(\tau_*^+). \quad (34)$$

Table 1: Impact scenarios of the planar lattice when the  $s$ -th layer is impacting at the time  $\tau_*$  ( $s, j = 1, 2$  with  $s \neq j$ )

Just before impact ( $\tau = \tau_*^-$ )		Just after impact ( $\tau = \tau_*^+$ )	
# Deformed layers	Condition	# Deformed layers	Condition
1	$\theta_s(\tau_*^-) \rightarrow 0,$ $\theta_j(\tau_*^-) = 0$	1	$\theta_s(\tau_*^+) = 0,$ $\theta_j(\tau_*^+) \neq 0$ <i>No Bouncing</i>
			$\theta_s(\tau_*^+) \neq 0,$ $\theta_j(\tau_*^+) = 0$ <i>Bouncing</i>
		2	$\theta_s(\tau_*^+) \neq 0,$ $\theta_j(\tau_*^+) \neq 0$ <i>Partial Bouncing</i>
2	$\theta_s(\tau_*^-) \rightarrow 0,$ $ \theta_j(\tau_*^-)  = \theta_* >  \theta_s(\tau_*^-) $	1	$\theta_s(\tau_*^+) = 0,$ $\theta_j(\tau_*^+) \neq \theta_*$ <i>No Bouncing</i>
		2	$\theta_s(\tau_*^+) \neq 0,$ $\theta_j(\tau_*^+) \neq \theta_*$ <i>Bouncing</i>

In analogy with other classical problems in physics (as, among others, the bouncing ball, the collision of rolling balls, vehicle collision, and rocking motion of rigid block on rigid surfaces), the structural system may lose part of (or even increase in the presence of external forces, as shown later) its energy during the impact (in the form of heat, noise, dissipation mechanisms, etc). Since the difference angles  $\theta_s$  and  $\theta_j$  are continuous, eqn. (31), the potential energy  $\Pi$ , eqn. (18), is continuous too and therefore the variation in the energy  $\mathcal{E} = \mathcal{T} + \Pi$  implies a variation only in the kinetic energy  $\mathcal{T}$ , eqn. (17). Following Housner [42], a restitution coefficient  $r$  can be introduced as the ratio between the kinetic energies just after and just before the impact,

$$r = \frac{\mathcal{T}(\tau_*^+)}{\mathcal{T}(\tau_*^-)} > 0, \quad (35)$$

so that the energy difference at the impact can be expressed as

$$\mathcal{E}(\tau_*^+) - \mathcal{E}(\tau_*^-) = \mathcal{T}(\tau_*^+) - \mathcal{T}(\tau_*^-) = -(1-r)\mathcal{T}(\tau_*^-). \quad (36)$$

In some impact problems, inherent assumptions about the motion define the value of the restitution coefficient  $r$ . For example, by assuming the pivoting point coincident with the impact point in the rocking motion of a rigid body, a closed form expression for  $r$  can be derived through the law of the conservation of the angular momentum [42]. However, the present structural system shows statically indeterminacy at the impact and therefore a closed-form expression for the restitution coefficient  $r$  can not be derived. An experimental campaign should be performed to effectively overcome the indeterminacy about the restitution coefficient, as well as the scenario disclosure after the impact. Since, experimental measures fall outside the scope of the present research, and these are anyway expected to be affected by the technical realization of the joints and sliders, and the material composing the structure, the following simplifying assumptions are made

- i. *no bouncing* of the impacting layer;
- ii. only one layer deformed at every time  $\tau$ .

Under the two previous assumptions, the inequality (10)<sub>3</sub> constraining the difference angles reduce to

$$\theta_1(\tau)\theta_2(\tau) = 0, \quad \forall \tau, \quad (37)$$

so that a unique angle measure  $\theta(\tau)$  can be introduced to describe in time the two difference angles as

$$\begin{cases} \theta_1(\tau) = \theta(\tau), \\ \theta_2(\tau) = 0, \end{cases} \quad \text{if } \theta(\tau) \geq 0, \quad \text{and} \quad \begin{cases} \theta_1(\tau) = 0, \\ \theta_2(\tau) = \theta(\tau), \end{cases} \quad \text{if } \theta(\tau) \leq 0, \quad (38)$$

and therefore

*by excluding bouncing, the present non-smooth two degrees of freedom system can be modeled as a non-smooth single degree of freedom system.*

More specifically, the two equations of motion (25) are equivalent to the following single equation of motion for  $\theta(\tau)$

$$\begin{aligned} (1+m)^{\mathbf{H}(\theta(\tau))} \ddot{\theta}(\tau) + c^{\mathbf{H}(\theta(\tau))} \mathcal{C} \dot{\theta}(\tau) + k^{\mathbf{H}(\theta(\tau))} \theta(\tau) = \\ \sin(|\theta(\tau)| + \beta_0) \left[ (1+h(\tau))^{\mathbf{H}(\theta(\tau))} \mathcal{H}(\tau) - (1+m)^{\mathbf{H}(\theta(\tau))} \ddot{\zeta}(\tau) \right] \\ + \text{sgn}[\theta(\tau)] \cos(|\theta(\tau)| + \beta_0) \left[ (1+v(\tau))^{\mathbf{H}(\theta(\tau))} \mathcal{V}(\tau) - (1+m)^{\mathbf{H}(\theta(\tau))} \ddot{\nu}(\tau) \right], \end{aligned} \quad (39)$$

with the sign, the absolute value, and the Heaviside step  $\mathbf{H}$  functions providing the discontinuous character at each impact time  $\tau_*$ , where  $\theta(\tau_*) = 0$ . The acceleration jump  $\llbracket \ddot{\theta}(\tau_*) \rrbracket$  at the impact can be evaluated from the equation of motion (39) as

$$\begin{aligned} \llbracket \ddot{\theta}(\tau_*) \rrbracket = \frac{\text{sgn}[\theta(\tau_*)]}{1+m} \{ & (h(\tau_*) - m)\mathcal{H}(\tau_*) \sin \beta_0 + (1-c+m)\mathcal{C} \llbracket \dot{\theta}(\tau_*) \rrbracket \\ & + [(m+v(\tau_*)+2)\mathcal{V}(\tau_*) - 2(1+m)\ddot{\nu}(\tau_*)] \cos \beta_0 \}, \end{aligned} \quad (40)$$

which shows that the non-smooth response of the system is not only deriving from the possible energy (or, equivalently, velocity) change at the impact, and therefore is present even in the case of kinetic energy (or velocity) continuous at the impact. Moreover, the jump acceleration is not affected by the horizontal ground acceleration  $\ddot{\zeta}$ .



In addition to non-smoothness, in general the system displays also no symmetry in the response. However, a symmetric behaviour in the horizontal load and ground motion can be recovered when the structural system is loaded only with forces at the top layer, ( $v(\tau) = h(\tau) = 0$ ), the mass is only present at the top layer ( $m = 0$ ), and the damping and stiffness are the same for the two layers ( $c = k = 1$ ). Indeed, under these assumptions the equation of motion (39) simplifies to<sup>4</sup>

$$\ddot{\theta}(\tau) + \mathcal{C} \dot{\theta}(\tau) + \theta(\tau) = \sin(|\theta(\tau)| + \beta_0) [\mathcal{H}(\tau) - \ddot{\zeta}(\tau)] + \operatorname{sgn}[\theta(\tau)] \cos(|\theta(\tau)| + \beta_0) [\mathcal{V}(\tau) - \ddot{\nu}(\tau)], \quad (42)$$

which implies that the rotation  $\theta(\tau)$  has the following symmetry in the horizontal load and ground motion (by keeping same vertical load and ground motion)

$$\theta(\tau)|_{\mathcal{H}(\tau), \zeta(\tau), \mathcal{V}(\tau), \nu(\tau)} = -\theta(\tau)|_{-\mathcal{H}(\tau), -\zeta(\tau), \mathcal{V}(\tau), \nu(\tau)}. \quad (43)$$

Under the considered symmetry assumption, the acceleration jump in eqn. (40) reduces into

$$[\ddot{\theta}(\tau_*)] = \operatorname{sgn}[\theta(\tau_*)] [\mathcal{C} [\dot{\theta}(\tau_*)] + 2 \cos \beta_0 [\mathcal{V}(\tau_*) - \ddot{\nu}(\tau_*)]], \quad (44)$$

confirming that the non-smooth character in the acceleration still persists, although dependent only on the vertical actions,  $\mathcal{V}(\tau)$  and  $\ddot{\nu}(\tau)$ , and not on the horizontal ones,  $\mathcal{H}(\tau)$  and  $\ddot{\zeta}(\tau)$ .

A further comment on the dissipation at the impact is needed before addressing eqn. (42) in the following Sections to analyse the non-smooth vibrations of the system under constant and varying loading conditions. In addition to the restitution factor  $r$ , the dissipation at the impact can be also expressed through the reduction factor  $e \in (0, 1]$ , which is the multiplier of the velocity just before the impact,  $\dot{\theta}(\tau_*^-)$ , to obtain that just after,  $\dot{\theta}(\tau_*^+)$ , namely

$$\dot{\theta}(\tau_*^+) = e \dot{\theta}(\tau_*^-). \quad (45)$$

By considering the kinetic energy  $\mathcal{T}$ , eqn. (17), the restitution factor  $r$  can be related to the reduction factor  $e$  as

$$r = \frac{\left[ e \dot{\theta}(\tau_*^-) \sin \beta_0 + \dot{\zeta}(\tau_*) \right]^2 + \left[ e \dot{\theta}(\tau_*^-) \cos \beta_0 + \dot{\nu}(\tau_*) \right]^2}{\left[ \dot{\theta}(\tau_*^-) \sin \beta_0 + \dot{\zeta}(\tau_*) \right]^2 + \left[ \dot{\theta}(\tau_*^-) \cos \beta_0 + \dot{\nu}(\tau_*) \right]^2}, \quad (46)$$

showing that the two factors can not be both assumed as constant values, except when both the ground velocities are null,

$$\dot{\zeta}(\tau_*) = \dot{\nu}(\tau_*) = 0 \quad \Rightarrow \quad r = e^2. \quad (47)$$

It is evident from eqn. (46) that a decrease of kinetic energy  $\mathcal{T}$  at the impact defines the two following equivalent constraints

$$r < 1 \quad \Longleftrightarrow \quad \left[ (1 + e) \dot{\theta}(\tau_*^-) + 2 \left( \dot{\zeta}(\tau_*) \sin \beta_0 + \dot{\nu}(\tau_*) \cos \beta_0 \right) \right] \dot{\theta}(\tau_*^-) > 0, \quad (48)$$

and therefore the condition  $e \in (0, 1)$  guarantees the energy reduction only in the case of null ground velocities, eqn. (47). The same phenomenon can be observed also in the classical problem of rocking motion of rigid bodies, which to our best knowledge has not been previously disclosed in literature [42, 43, 44, 45, 46, 47, 48, 49]. Indeed, as shown in the next Section, the present system displays some similarities with the rocking motion of rigid bodies in terms of energy balance and behaviour at the impact instant, but it is fundamentally different

<sup>4</sup>It is interesting to note that the non-smooth structural system under consideration reduces to an inverted (smooth) pendulum constrained by a linear elastic torsional spring when the undeformed configuration angle is taken as  $\beta_0 = \pi/2$ ,

$$\ddot{\theta}(\tau) + \mathcal{C} \dot{\theta}(\tau) + \theta(\tau) = \cos \theta(\tau) [\mathcal{H}(\tau) - \ddot{\zeta}(\tau)] - \sin \theta(\tau) [\mathcal{V}(\tau) - \ddot{\nu}(\tau)]. \quad (41)$$

for its multistable nature due to presence of restoring forces enabled by the visco-elastic hinges (more details on the energy balance of the rocking rigid body and its similarities with the present system are provided in Appendix A).

In conclusion, the non-smoothness of the present system appears at every impact time ( $\tau_*$ ) and in particular:

- a jump in the acceleration  $\llbracket \ddot{\theta}(\tau_*) \rrbracket$ , inherent to the non linearity of the governing equation, is always present;
- a jump in the velocity  $\llbracket \dot{\theta}(\tau_*) \rrbracket$  may be introduced to represent dissipation mechanisms at impact (as, for example, through the reduction factor  $e$ ).

The system is analysed under different loading conditions in the following Sections. First, in order to provide an insight into the influence of the velocity reduction factor, the system has been analysed in Sect. 5 under constant loading conditions with constant reduction factor less than the unit  $e < 1$ , which as it has been shown in the literature of rocking motion [50, 51, 52, 53, 54], remains the best approach to introduce the damping mechanism under non-varying loadings. Then, the analysis is extended in Sect. 6 to loading conditions varying in time by modelling the dissipation mechanisms through viscous damping only (therefore taking a unit reduction factor,  $e = 1$ ), because of the large number of parameters present in the model.

## 5 Vibrations at constant vertical loading

Under a constant vertical load, while all the other forces and the ground motion are null, and for symmetric linear damping

$$\mathcal{V}(\tau) = \bar{\mathcal{V}}, \quad \mathcal{H}(\tau) = v(\tau) = \ddot{\zeta}(\tau) = \ddot{v}(\tau) = 0, \quad c = 1, \quad (49)$$

the equation of motion (39) reduces to

$$(1 + m)^{H(\theta(\tau))} \ddot{\theta}(\tau) + \mathcal{C} \dot{\theta}(\tau) + k^{H(\theta(\tau))} \theta(\tau) = \text{sgn}[\theta(\tau)] \cos(|\theta(\tau)| + \beta_0) \bar{\mathcal{V}}, \quad (50)$$

and the (dimensionless) potential energy  $\mathcal{P}(\theta)$  can be evaluated as the elastic energy stored in the deformed spring and the potential of the load as

$$\mathcal{P}(\theta) = k^{H(\theta)} \frac{\theta^2}{2} + \bar{\mathcal{V}} [\sin \beta_0 - \sin(\beta_0 + |\theta|)]. \quad (51)$$

It is interesting to note that by considering a symmetric system with null damping ( $k = 1$ ,  $\mathcal{C} = m = 0$ ), eqn. (39) can be rewritten as

$$\ddot{\theta}(\tau) + \theta(\tau) = -\text{sgn}[\theta(\tau)] \bar{\mathcal{V}} \sin\left(\beta_0 - \frac{\pi}{2} + |\theta(\tau)|\right), \quad (52)$$

which differs from the celebrated equation of the free rocking motion for rigid bodies obtained by Housner in 1963 [42] only for the presence of the linear term in rotation related to the rotational springs (further details are provided in Appendix A).

The dynamics under constant vertical loading and no-bouncing assumption is investigated in this Section through small amplitude vibrations analysis, phase portraits for large amplitude vibrations, and through the realization of a bouncing-like motion from extreme non-symmetric systems.

### 5.1 Small amplitude vibrations

Expansion at the first order for small amplitude rotation  $\theta(\tau)$  provides the following nonhomogeneous differential equation with non-constant coefficients

$$(1 + m)^{H(\theta(\tau))} \ddot{\theta}(\tau) + \mathcal{C} \dot{\theta}(\tau) + (\bar{\mathcal{V}} \sin \beta_0 + k^{H(\theta(\tau))}) \theta(\tau) = \text{sgn}[\theta(\tau)] \bar{\mathcal{V}} \cos \beta_0, \quad (53)$$

which, by considering that the rotation is continuous in time, consists in a nonhomogeneous piecewise-linear differential equation with constant coefficients, which is expressed dependently on the rotation sign as

$$\begin{cases} \ddot{\theta}(\tau) + 2\mu_1\Omega_0^{[1]}\dot{\theta}(\tau) + \left(\Omega_0^{[1]}\right)^2\theta(\tau) = \frac{\bar{V}\cos\beta_0}{1+m}, & \text{for } \theta(\tau) > 0, \\ \ddot{\theta}(\tau) + 2\mu_2\Omega_0^{[2]}\dot{\theta}(\tau) + \left(\Omega_0^{[2]}\right)^2\theta(\tau) = -\bar{V}\cos\beta_0, & \text{for } \theta(\tau) < 0, \end{cases} \quad (54)$$

where  $\Omega_0^{[p]}$  and  $\mu_p$  are respectively the ‘apparent’ angular frequency and the damping ratio,

$$\begin{aligned} \Omega_0^{[1]} &= \sqrt{\frac{k + \bar{V}\sin\beta_0}{1+m}}, \quad \mu_1 = \frac{\mathcal{C}}{2\sqrt{1+m}\sqrt{k + \bar{V}\sin\beta_0}}, \\ \Omega_0^{[2]} &= \sqrt{1 + \bar{V}\sin\beta_0}, \quad \mu_2 = \frac{\mathcal{C}}{2\sqrt{1 + \bar{V}\sin\beta_0}}. \end{aligned} \quad (55)$$

Since the derivative of the (dimensionless) potential energy (51) can be approximated as

$$\frac{d\mathcal{P}(\theta)}{d\theta} \approx \left(k^{\mathcal{H}(\theta)} + \bar{V}\sin\beta_0\right)\theta - \text{sgn}[\theta]\bar{V}\cos\beta_0. \quad (56)$$

the stability of the undeformed equilibrium configuration is assessed as

$$\theta = 0 \text{ is } \left\{ \begin{array}{c} \text{stable} \\ \text{unstable} \end{array} \right\} \text{ equilibrium if } \bar{V}\cos\beta_0 \left\{ \begin{array}{c} < 0, \\ > 0. \end{array} \right. \quad (57)$$

In addition to the undeformed equilibrium state  $\theta(\tau) = 0$ , two adjacent equilibrium states  $\theta(\tau) = \theta_A > 0$  and  $\theta(\tau) = \theta_B < 0$  can be evaluated from eqn. (54) as

$$\theta_A = \frac{\bar{V}\cos\beta_0}{k + \bar{V}\sin\beta_0} > 0, \quad \theta_B = -\frac{\bar{V}\cos\beta_0}{1 + \bar{V}\sin\beta_0} < 0, \quad (58)$$

which are unstable (or stable) when the undeformed state is stable (or unstable). Indeed, the constraint about positive  $\theta_A$  and negative  $\theta_B$  together with the condition for a stable undeformed state ( $\bar{V}\cos\beta_0 < 0$ ) leads to the following constraint

$$\min\{1, k\} + \bar{V}\sin\beta_0 < 0 \quad \Rightarrow \quad \bar{V} < -\frac{\min\{1, k\}}{\sin\beta_0}, \quad (59)$$

which implies a positive sign in the potential energy differences

$$\mathcal{P}(\theta_A) - \mathcal{P}(0) \approx -\frac{\bar{V}^2\cos^2\beta_0}{2(k + \bar{V}\sin\beta_0)} > 0, \quad \mathcal{P}(\theta_B) - \mathcal{P}(0) \approx -\frac{\bar{V}^2\cos^2\beta_0}{2(1 + \bar{V}\sin\beta_0)} > 0, \quad (60)$$

and therefore the instability of the corresponding deformed equilibrium states.

Due to the nature of the small vibration analysis, the two equilibrium configurations  $\theta_A$  and  $\theta_B$  are relevant only when their modulus is small, condition appearing only if  $\beta_0 \approx \pi/2$ , for which

$$\theta_A \approx \frac{\bar{V}}{k + \bar{V}} \left(\frac{\pi}{2} - \beta_0\right), \quad \theta_B \approx -\frac{\bar{V}}{1 + \bar{V}} \left(\frac{\pi}{2} - \beta_0\right), \quad (61)$$

under the constraint (59), which reduces to

$$\bar{V} < -\min\{1, k\}. \quad (62)$$

Overall, recalling the restriction  $\beta_0 \in (0, \pi)$ , considering null initial velocity ( $\dot{\theta}(0) = 0$ ) and a non-null position ( $\theta(0) = \theta_0 \neq 0$ ), a divergent motion (under small rotations) is realized from the undeformed state  $\theta = 0$  in the following cases

- when  $\beta_0 \neq \frac{\pi}{2}$  if  $\bar{\mathcal{V}}\left(\frac{\pi}{2} - \beta_0\right) > 0$ ;
- when  $\beta_0 \rightarrow \left(\frac{\pi}{2}\right)^-$  if  $\bar{\mathcal{V}}\left(\frac{\pi}{2} - \beta_0\right) < 0$  and in addition if  $\bar{\mathcal{V}} < -k$  by taking  $\theta_0 > \theta_A$  and if  $\bar{\mathcal{V}} < -1$  by taking  $\theta_0 < \theta_B$ ;
- when  $\beta_0 = \frac{\pi}{2}$  if  $\bar{\mathcal{V}} < -k$  by taking  $\theta_0 > 0$  and if  $\bar{\mathcal{V}} < -1$  by taking  $\theta_0 < 0$ .

Recalling the solution from linear oscillators under constant force and with a subcritical damping ( $\{\mu_1, \mu_2\} < 1$ ), the vibrations in time are expressed for initial non-null rotation and null velocity ( $\theta_0 \neq 0$  and  $\dot{\theta}_0 = 0$ ) by

$$\theta(\tau) = e^{-\mu_p \Omega_0^{[p]} \tau} \left[ A_i \cos \left( \sqrt{1 - \mu_p^2} \Omega_0^{[p]} \tau \right) + B_i \sin \left( \sqrt{1 - \mu_p^2} \Omega_0^{[p]} \tau \right) \right] + (-1)^i \text{sgn}[\theta_0] \frac{\bar{\mathcal{V}} \cos \beta_0}{k^{2-p} + \bar{\mathcal{V}} \sin \beta_0}, \quad (63)$$

$$\text{with } p = \frac{3 - (-1)^i \text{sgn}[\theta_0]}{2}, \quad \text{for } \tau \in \left( \tau_*^{[i]}, \tau_*^{[i+1]} \right), \quad i \in \mathbb{N}_0,$$

where  $\tau_*^{[0]} = 0$ ,  $\tau_*^{[i]}$  represents the time when the  $i$ -th (non-bouncing) impact occurs ( $i \in \mathbb{N}$ ), while  $A_i$  and  $B_i$  are integration constants defining the motion before the  $(i+1)$ -th impact and after the previous one to be evaluated as iterative procedure starting from the initial conditions,  $\theta(0) = \theta_0$  and  $\dot{\theta}(0) = 0$ , for  $i = 0$  and following the condition of continuous rotation and discontinuous velocity at the  $i$ -th impact for  $i \geq 1$ , given by

$$\theta \left( \tau_*^{[i]-} \right) = \theta \left( \tau_*^{[i]+} \right) = 0, \quad \dot{\theta} \left( \tau_*^{[i]+} \right) = e \dot{\theta} \left( \tau_*^{[i]-} \right), \quad i \in \mathbb{N}. \quad (64)$$

Restricting the attention to undamped symmetric systems ( $m = \mathcal{C} = 0$ ,  $k = 1$ ), for which  $\Omega_0^{[p]} = \Omega_0$  and  $\mu_p = 0$  ( $p = 1, 2$ ), the small vibrations at constant vertical loading reduce to

$$\theta(\tau) = A_i \cos(\Omega_0 \tau) + B_i \sin(\Omega_0 \tau) + (-1)^i \text{sgn}[\theta_0] \frac{\bar{\mathcal{V}} \cos \beta_0}{1 + \bar{\mathcal{V}} \sin \beta_0}, \quad \text{for } \tau \in \left( \tau_*^{[i]}, \tau_*^{[i+1]} \right), \quad i \in \mathbb{N}_0, \quad (65)$$

with the two non-trivial equilibrium rotations (58) becoming

$$\theta_A = -\theta_B = \frac{\bar{\mathcal{V}} \cos \beta_0}{1 + \bar{\mathcal{V}} \sin \beta_0}, \quad (66)$$

which are relevant only when  $\beta_0 \approx \pi/2$  and are unstable when

$$\bar{\mathcal{V}} < -1. \quad (67)$$

By assuming that the dissipation does not appear even at the impact ( $e = 1$ ), the motion becomes periodic with a dimensionless period  $T_0$ , different from  $2\pi/\Omega_0$  whenever  $\bar{\mathcal{V}} \neq 0$ , given by

$$T_0(\theta_0) = \frac{4}{\sqrt{1 + \bar{\mathcal{V}} \sin \beta_0}} \arccos \left( \frac{1}{1 - \frac{1 + \bar{\mathcal{V}} \sin \beta_0}{\bar{\mathcal{V}} \cos \beta_0} |\theta_0|} \right), \quad (68)$$

which, from its expansion at small rotation ( $\theta_0 \approx 0$ ), under the constraint  $|\theta_0| \ll |\bar{\mathcal{V}} \cos \beta_0 / (1 + \bar{\mathcal{V}} \sin \beta_0)|$ , for  $\beta_0 \neq \pi/2$  results proportional to the square root of the initial perturbation  $\theta_0$ , similarly to the dynamics of a rocking rigid body [42] (see Appendix A)

$$T_0(\theta_0) \approx \frac{4\sqrt{2|\theta_0|}}{\sqrt{-\bar{\mathcal{V}} \cos \beta_0}}, \quad (69)$$

confirming the inequality (57) for having no divergent motion from the undeformed state  $\theta = 0$ . Moreover, in the case when  $\beta_0 \approx \pi/2$ , the non-trivial equilibrium configuration can be approximated by  $\theta_A \approx (\pi/2 - \beta_0) \bar{\mathcal{V}}/(1 + \bar{\mathcal{V}})$  and the following expansion for the dimensionless period  $T_0$  can be obtained

$$T_0(\theta_0) \approx \frac{4}{\sqrt{1 + \bar{\mathcal{V}}}} \arccos \left[ \frac{1}{1 - \frac{1 + \bar{\mathcal{V}}}{\bar{\mathcal{V}}} \frac{|\theta_0|}{\frac{\pi}{2} - \beta_0}} \right], \quad (70)$$

further confirming that the divergent motion (under the small rotation assumption) from the undeformed state ( $\theta = 0$ ) is realized under the conditions obtained from the potential energy analysis discussed before.

Extending now the small amplitude vibrations to the presence of impact dissipation ( $e \leq 1$ ), the oscillations lose periodicity by decreasing amplitude and period after every impact. Indeed, through energy balance, the (small) oscillation amplitude  $\theta_D^{\{n\}} = \theta \left( \tau_*^{[2(n-1)]} \right)$  at the beginning of the  $n$ -th oscillation (occurring from  $\tau_*^{[2(n-1)]}$  and  $\tau_*^{[2(n)]} = \tau_*^{[2(n-1)]} + T_D^{\{n\}}$ , therefore encompassing two impacts,  $n \in \mathbb{N}$ ) can be approximated as

$$\theta_D^{\{n\}} \approx e^{4n} \theta_0, \quad (71)$$

while the  $n$ -th cycle period  $T_D^{\{n\}}$  can be approximated by<sup>5</sup>

$$T_D^{\{n\}} \approx e^{2(n-1)} T_D^{\{1\}}, \quad \text{with} \quad T_D^{\{1\}} \approx \frac{(1+e)^2}{4} T_0 \leq T_0, \quad (72)$$

showing the decrease of both the amplitude  $\theta_D^{\{n\}}$  and period  $T_D^{\{n\}}$  with the increasing number of impact cycles, similarly to the rocking motion of rigid bodies. More specifically, it is noted that the period  $T_D^{\{n\}}$  approaches zero in the limit of infinite number  $n$  of oscillations and, interestingly, the oscillatory motion ends at a finite time  $\tau_{\text{fin}}$ , because the corresponding time  $\tau_*^{[2n]}$  for infinite  $n$  is given by the following convergent geometric series (for  $e < 1$ )

$$\tau_{\text{fin}} = \lim_{n \rightarrow \infty} \tau_*^{[2n]} = \sum_{p=1}^{\infty} T_D^{\{p\}} \approx \frac{1+e}{4(1-e)} T_0. \quad (73)$$

## 5.2 Phase portraits of vibrations at large amplitude

The vibrations for a system under a constant vertical loading are here addressed without any restriction about small rotations. The analysis is referred to a system with  $\beta_0 = 80^\circ$  and loaded only with a constant vertical load  $\bar{\mathcal{V}} = -1.5/\sin \beta_0 \approx -1.523$ , realizing multistability through three<sup>6</sup> stable equilibrium states ( $\theta = 0$ ,  $\theta = \theta_I > 0$  and  $\theta = \theta_{II} < 0$ ), while for simplicity a null mass ratio is assumed ( $m = 0$ ). Considering specific initial rotation and velocity, the numerical integration of the equation of motion (50) can be performed and the trajectories within the phase plane  $\theta - \dot{\theta}$  defined. These trajectories show how the motion evolves in time and in particular allows for the definition of *separatrices*, namely lines separating conditions in regions corresponding to qualitatively different motion. Moreover, all the trajectories display a discontinuity in their tangent when crossing the switching condition  $\theta = 0$ .

The phase portraits for a symmetric system ( $k=1$ , for which  $\theta_I = -\theta_{II} = 1.462$ ) are reported in Fig. 4 with varying the dissipation source, more specifically:

<sup>5</sup>Since the oscillation period decreases as effect of each impact, the time interval between two impacts decreases too, namely

$$\tau_*^{[2n]} - \tau_*^{[2n-1]} < \tau_*^{[2n-1]} - \tau_*^{[2(n-1)]}, \quad n \in \mathbb{N}.$$

<sup>6</sup>It is noted that the tetrastability presented in [38] reduces here to tristability because of the assumption about no more than one deformed layer at any time.

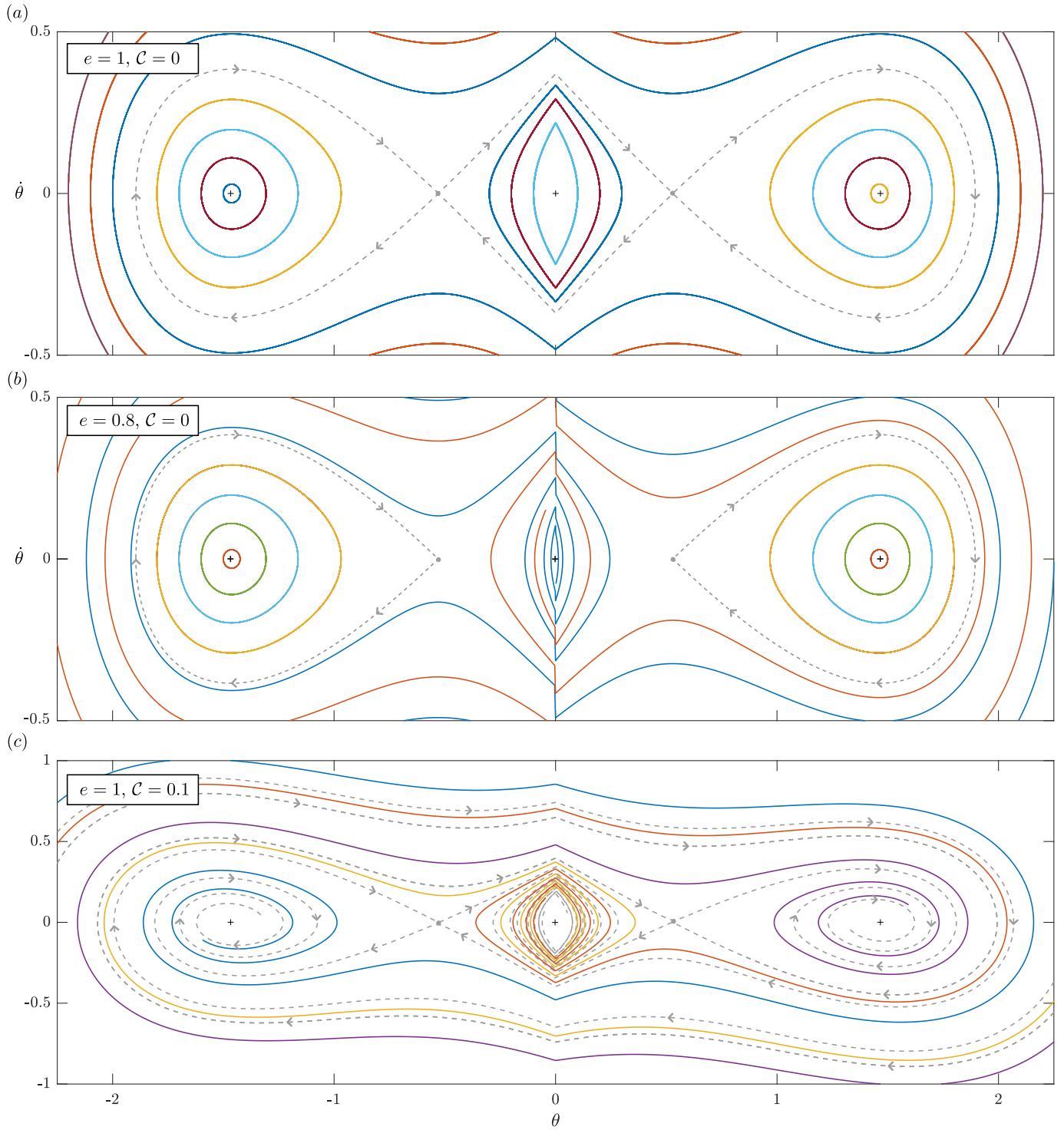


Figure 4: Phase portrait  $\theta(\tau) - \dot{\theta}(\tau)$  for the symmetric system ( $k = 1, m = 0$ ) under a constant vertical load  $\bar{\mathcal{V}} = -1.523$  and for  $\beta_0 = 80^\circ$  with varying dissipation source: (a) no dissipation ( $e = 1, \mathcal{C} = 0$ ), (b) dissipation through impact only ( $e = 0.8, \mathcal{C} = 0$ ), and (c) dissipation through viscous damping only ( $e = 1, \mathcal{C} = 0.1$ ).

Fig. 4 a) no dissipation ( $\mathcal{C} = 0, e = 1$ ). The system is conservative and the phase portrait is symmetric with respect to both the  $\theta$  and  $\dot{\theta}$  axes. The separatrices (reported as dashed gray line) define three bounded regions, each one containing one attractor (equilibrium configuration) only. Therefore,



the periodic oscillating motion is around only one attractor if the initial condition is within the corresponding separatrix curve, otherwise around all of the three attractors if the condition is outside;

Fig. 4 b) dissipation through impact only ( $\mathcal{C} = 0, e = 0.8$ ). With respect to the previous conservative case, the trajectories are modified only when crossing the switching condition ( $\theta = 0$ ), where a jump discontinuity appears. It follows that the portion of separatrix line bounding the region encompassing the attractor at the origin ( $\theta = 0$ ) disappears and the related region merges with the unbounded one to generating a decaying motion towards the undeformed configuration, while the other two bounded regions still define periodic motion around the respective non-trivial attractor ( $\theta = \theta_I$  and  $\theta = \theta_{II}$ ) and remain unaffected;

Fig. 4 c) dissipation through viscous damping only ( $\mathcal{C} = 0.1, e = 1$ ). By considering that energy is continuously dissipated in time, every trajectory defines a decaying (non-periodic) oscillatory motion towards one of the three attractors. Therefore, differently from the two previous cases, no trajectory is bounded and, although approaching a different attractor at infinite time, each trajectory describes oscillations around all of the three attractors for some time interval.

For completeness, the response for a conservative non-symmetric system ( $\mathcal{C} = 0, e = 1$ ) is shown in Fig. 5 for two different values of stiffness ratio  $k$ .

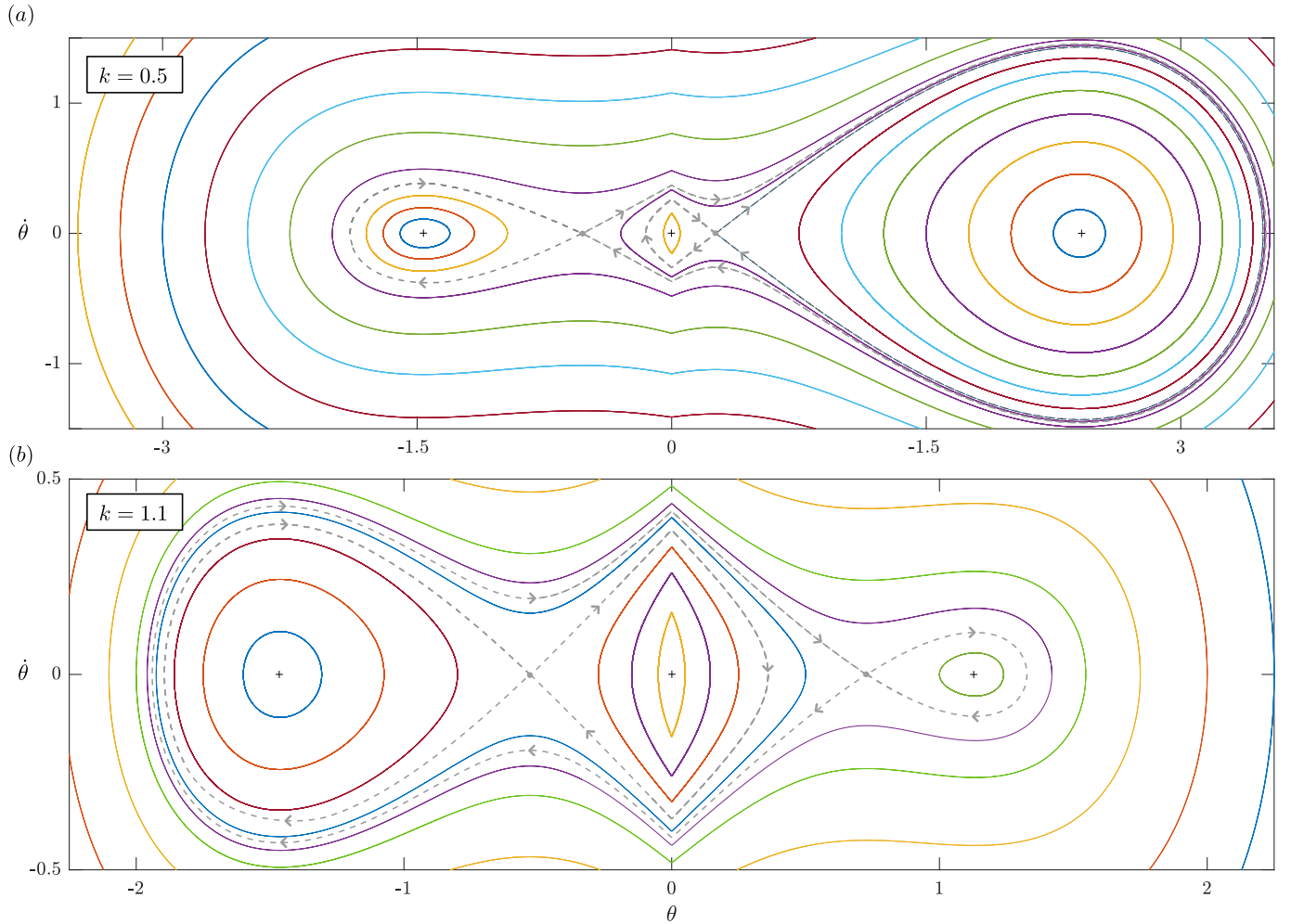


Figure 5: Phase portrait  $\theta(\tau) - \dot{\theta}(\tau)$  for non-symmetric conservative systems ( $e = 1, m = \mathcal{C} = 0$ ) under a constant vertical load  $\bar{\mathcal{V}} = -1.523$  and for  $\beta_0 = 80^\circ$  with varying stiffness ratio: (a)  $k = 0.5$  and (b)  $k = 1.1$ .

With respect to the symmetric ( $k = 1$ ) case, only the portion of trajectories within the half-plane  $\theta > 0$ , and correspondingly the positive equilibrium configuration  $\theta_I$ , is modified. In particular:

Fig. 5 a) lower layer softer than the upper one ( $k = 0.5$ ). The positive value of non-trivial equilibrium increases ( $\theta_I = 2.405$ ) as the size of the region defined by the separatrix encompassing it;

Fig. 5 b) lower layer stiffer than the upper one ( $k = 1.1$ ). The positive value of non-trivial equilibrium decreases ( $\theta_I = 1.384$ ) and, as a consequence, the corresponding separatrix region shrinks.

Moreover, differently from the conservative symmetric case ( $k = e = 1$ ,  $\mathcal{C} = 0$ ), the separatrices in the conservative non-symmetric system show the possibility of periodic oscillations around two (instead of only one or three) equilibrium configurations, corresponding to  $\theta_I$  when  $k < 1$  ( $\theta_{II}$  when  $k > 1$ ) and  $\theta = 0$ .

### 5.3 Bouncing-like motion from extreme non-symmetric systems under no-bouncing assumption

Despite the no-bouncing assumption at impact, non-symmetric systems may display a bouncing-like motion when characterized by extreme stiffness ratio. For the sake of simplicity, this behaviour is shown by analyzing conservative systems, therefore in absence of any dissipative mechanism ( $e = 1$ ,  $\mathcal{C} = 0$ ) and loadings varying in time, although these are not expected to qualitatively modify the response. It follows that the total energy is conserved and the motion is periodic, therefore defining the maximum and minimum rotations as

$$\theta_{\min} = \min_{\tau} \{\theta(\tau)\} < 0, \quad \theta_{\max} = \max_{\tau} \{\theta(\tau)\} > 0, \quad (74)$$

where velocity annihilates, the total energy matching at these two states reduces to the following (dimensionless) potential energy matching

$$k \frac{\theta_{\min}^2}{2} - \bar{\mathcal{V}} \sin(\beta_0 + \theta_{\min}) = \frac{\theta_{\max}^2}{2} - \bar{\mathcal{V}} \sin(\beta_0 - \theta_{\max}), \quad (75)$$

establishing a nonlinear relation between the maximum and minimum rotation values,  $\theta_{\max}$  and  $\theta_{\min}$ . Introducing the parameter  $P_R$  representing the peak ratio and defined as

$$P_R(\bar{\mathcal{V}}, k) = \min \left\{ \frac{\theta_{\max}}{|\theta_{\min}|}, \frac{|\theta_{\min}|}{\theta_{\max}} \right\} \in [0, 1], \quad (76)$$

a bouncing-like motion is realized in the limit of vanishing  $P_R$ .

It is noted that, from the energy balance (75), the peak ratio  $P_R$  satisfies the following identity

$$P_R(\bar{\mathcal{V}}, k) \Big|_{\theta_{\min} = -|\theta_0|} = P_R\left(\frac{\bar{\mathcal{V}}}{k}, \frac{1}{k}\right) \Big|_{\theta_{\max} = |\theta_0|}, \quad k \geq 1. \quad (77)$$

**Null vertical load  $\bar{\mathcal{V}} = 0$ .** When the vertical load is absent, the equation of motion (50) becomes homogeneous,

$$(1 + m)^{H(\theta(\tau))} \ddot{\theta}(\tau) + k^{H(\theta(\tau))} \theta(\tau) = 0, \quad (78)$$

and the energy matching (75) leads to

$$\theta_{\max} = -\sqrt{k} \theta_{\min}, \quad (79)$$

from which the peak ratio  $P_R$  can be analytically evaluated as

$$P_R(k) = \min \left\{ \frac{1}{\sqrt{k}}, \sqrt{k} \right\}. \quad (80)$$

Likewise, the period of oscillation  $T_0$ , in terms of the dimensionless time  $\tau = t\sqrt{M_2/K_2}$ , is given by the sum of the time duration  $T_0^{[1]}$  of the oscillation for positive rotation and by  $T_0^{[2]}$  for the negative ones, respectively given by

$$T_0^{[1]}(k, m) = \pi\sqrt{\frac{m+1}{k}}, \quad T_0^{[2]} = \pi, \quad (81)$$

and therefore the period of oscillation  $T_0$  follows as

$$T_0(k, m) = \pi \left( 1 + \sqrt{\frac{m+1}{k}} \right). \quad (82)$$

It can be observed from eqn. (80) that the peak ratio  $P_R$  vanishes when the stiffness ratio  $k$  takes extremely small or large values,

$$\lim_{k \rightarrow 0} P_R(k) = \lim_{k \rightarrow \infty} P_R(k) = 0, \quad (83)$$

resembling a bouncing-like motion.

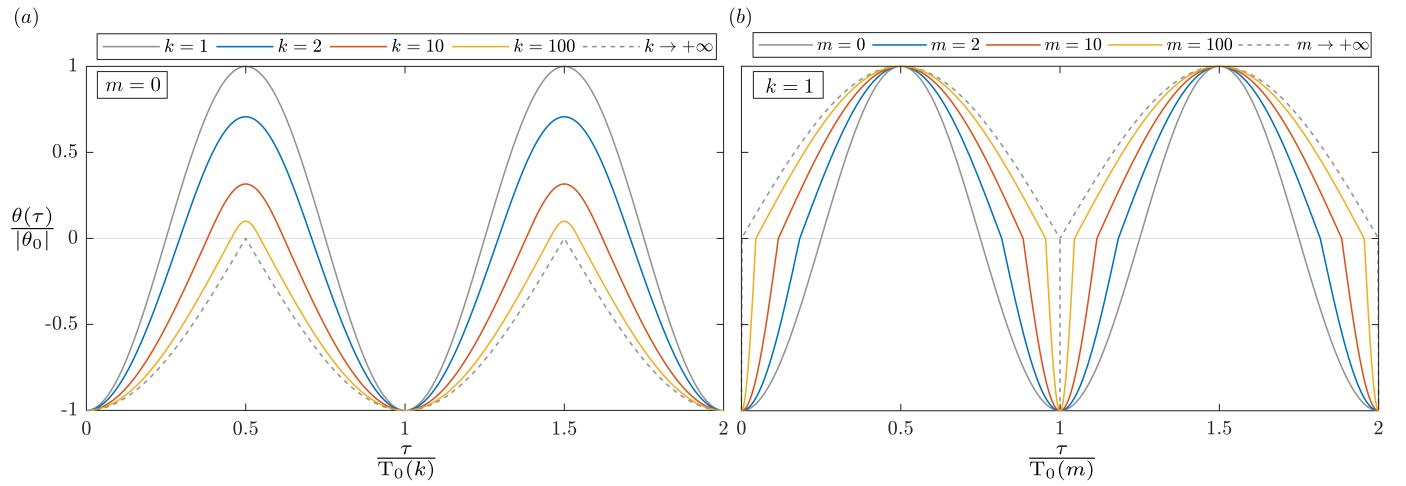


Figure 6: Time histories  $\theta - \tau/T_0(k, m)$  of a conservative system ( $\mathcal{C} = 0$ ,  $e = 1$ ) with  $\beta_0 = 80^\circ$ , under null vertical and horizontal loads, and with (a) stiffness ratio  $k \geq 1$  and null mass ratio  $m = 0$  and (b) unit stiffness ratio  $k = 1$  and non-null mass ratio  $m \geq 0$ .

It is interesting to observe that the corresponding periods of oscillation  $T_0$  are coincident with the oscillation time corresponding to only one (among the two) sign of rotation,

$$\begin{aligned} \lim_{k \rightarrow 0} \frac{T_0^{[2]}}{T_0^{[1]}(k, m)} = 0 & \Rightarrow \lim_{k \rightarrow 0} T_0 = \lim_{k \rightarrow 0} T_0^{[1]}(k, m) \rightarrow \infty, \\ \lim_{k \rightarrow \infty} \frac{T_0^{[1]}(k, m)}{T_0^{[2]}} = 0 & \Rightarrow \lim_{k \rightarrow \infty} T_0 = T_0^{[2]} = \pi. \end{aligned} \quad (84)$$

It is worth to mention that the infinite period of oscillation  $T_0$  at vanishing stiffness ratio  $k$  appears only because of the adopted time normalization (namely, with respect to  $K_2$  and  $M_2$  instead of  $K_1$  and  $M_1$ ). It also interesting to note that, although  $m$  does not affect the peak ratio  $P_R$ , extremely large values of  $m$  define vanishing duration of oscillations for negative sign of  $\theta(\tau)$ , namely

$$\lim_{m \rightarrow \infty} \frac{T_0^{[2]}}{T_0^{[1]}(k, m)} = 0 \Rightarrow \lim_{m \rightarrow \infty} T_0 = \lim_{m \rightarrow \infty} T_0^{[1]}(k, m) \rightarrow \infty. \quad (85)$$

Therefore, the case of large values of  $m$  (at finite values of  $k$ ) does not represent a real bouncing-like motion, although the oscillation phase involving negative rotation has vanishing duration and therefore it can be interpreted as an impulse to the system in the proper timescale. By considering only one source of non-symmetry in terms of stiffness ( $k \geq 1$ ,  $m = 0$ ) or mass ( $k = 1$ ,  $m \geq 0$ ) ratio, the rotation as a function of the dimensionless time  $\tau/T_0(k, m)$  is reported in Fig. 6 for  $\beta_0 = 80^\circ$ . The case  $k < 1$  is not reported since it is essentially the mirrored version of Fig. 6-a) about the (logarithmic) horizontal axis of the case with the corresponding reciprocal stiffness  $1/k > 1$ , as described by (77).

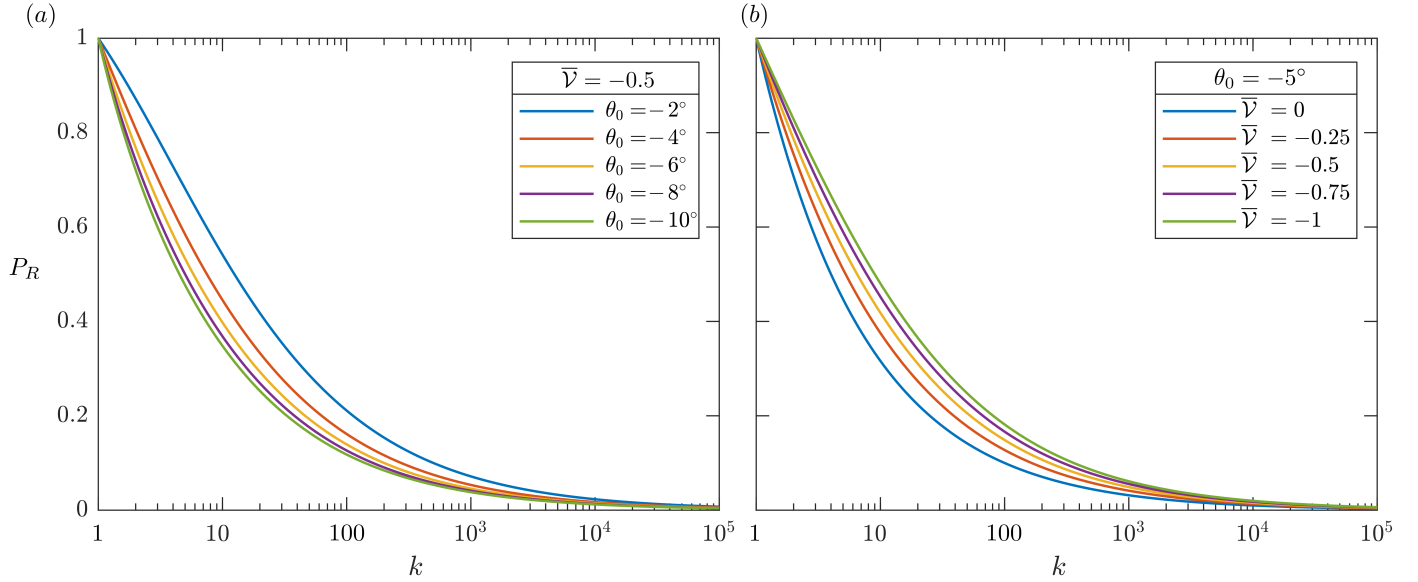


Figure 7: Peak ratio  $P_R$  for a conservative system ( $\mathcal{C} = 0$ ,  $e = 1$ ) with  $\beta_0 = 80^\circ$ ,  $m = v = c = 0$  at varying the stiffness ratio  $k \geq 1$  for (a) a vertical load  $\bar{V} = -0.5$  and different values of the initial rotation  $\theta_0 = -\{2, 4, 6, 8, 10\}^\circ$  and (b) an initial rotation  $\theta_0 = -5^\circ$  and different constant vertical loads  $\bar{V} = -\{0, 0.25, 0.5, 0.75, 1\}$ .

**Non-null constant vertical load  $\bar{V} < 0$ .** The realization of the bouncing-like motion in the case of extreme stiffness ratio values  $k$  is here shown to occur also in the presence of a negative vertical load ( $\bar{V} < 0$ ). In this case, the peak ratio  $P_R$  can be obtained only numerically by solving the nonlinear energy matching (75). The peak ratio  $P_R$  for a conservative system ( $\mathcal{C} = 0$ ,  $e = 1$ ,  $\beta_0 = 80^\circ$ ) is reported in Fig. 7 with varying the stiffness ratio  $k$  for (a) constant vertical load  $\bar{V} = -0.5$  and different initial rotation  $\theta_0 < 0$  and for (b) constant initial rotation  $\theta_0 = -5^\circ$  and different vertical loads  $\bar{V}$ . In both cases, the monotonic decrease of  $P_R$  is observed at increasing values of the stiffness ratio  $k \geq 1$ . Therefore the peak ratio approaches null values, representing a bouncing-like motion, in the limit of infinitely large stiffness ratio,  $P_R(\bar{V}, k \rightarrow \infty) = 0$ . Due to the symmetry property (77), a bouncing-like motion is also realized in the limit of vanishing stiffness ratio,  $\lim_{k \rightarrow 0} P_R(k\bar{V}, k) = 0$ .

## 6 Vibrations under loading varying in time

The vibrations of the symmetric system ( $m = v(\tau) = h(\tau) = 0$ ,  $k = c = 1$ ) dissipated through viscous damping only ( $\mathcal{C} > 0$ ,  $e = 1$ ) are analysed under different harmonic loads. In particular, the results are obtained through the numerical integration of the eqn. (42) under the following loading conditions:

- i. Harmonic horizontal load at constant vertical load (Fig. 8-a)

$$\mathcal{V}(\tau) = \bar{V}, \quad \mathcal{H}(\tau) = \hat{\mathcal{H}} \sin(\Omega\tau), \quad (86)$$

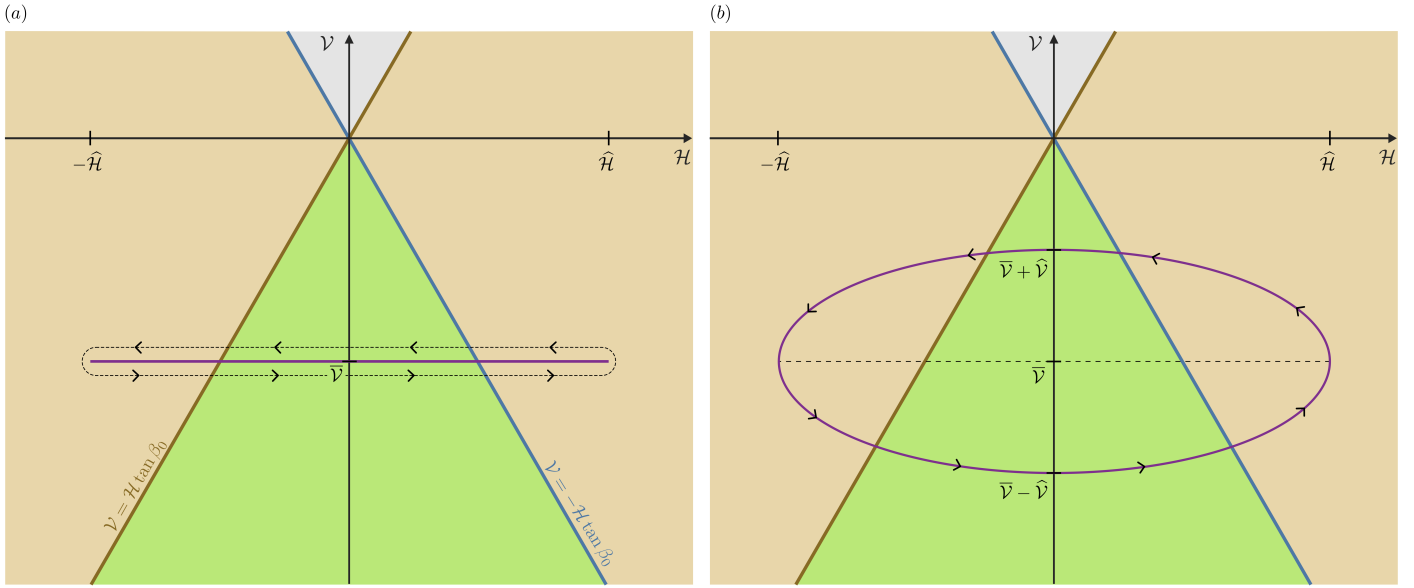


Figure 8: Loading paths in time within the  $\mathcal{H}$ - $\mathcal{V}$  plane for (a) harmonic horizontal force at constant vertical load  $\bar{\mathcal{V}}$ , eqn. (86), and (b) harmonic horizontal and vertical loads, eqn. (88). By modifying the loading amplitudes, the loading paths are considered within or intersecting the quasi-static monostable domain associated with the undeformed configuration (and reported in the sketch for  $\beta_0 \in (0, \pi/2)$ ), defined by the loading pairs satisfying  $\mathcal{V} \cos \beta_0 < -|\mathcal{H}| \sin \beta_0$ .

ii. Harmonic horizontal ground motion at constant vertical load

$$\mathcal{V}(\tau) = \bar{\mathcal{V}}, \quad \zeta(\tau) = \hat{\zeta} \sin(\Omega\tau), \quad (87)$$

which, from eqn. (42), is equivalent to loading condition (i.) by considering  $\hat{\mathcal{H}} = -\Omega^2 \hat{\zeta}$ ,

iii. Harmonic horizontal and vertical force at the second layer (Fig. 8-b)

$$\mathcal{H}(\tau) = \hat{\mathcal{H}} \sin(\Omega\tau) \quad \mathcal{V}(\tau) = \bar{\mathcal{V}} + \hat{\mathcal{V}} \cos(\Omega\tau). \quad (88)$$

Unless otherwise specified throughout the Section, the constant vertical load applied on the second layer is assumed as  $\bar{\mathcal{V}} = -0.5$  the initial configuration angle as  $\beta_0 = 80^\circ$  and the linear viscous damping as  $\mathcal{C} = 0.1$ . The remaining parameters of loading conditions are specified in the relevant parts of the text.

The dynamic behaviour of the unit structural cell is investigated in terms of frequency response curves and bifurcation diagrams, obtained from the numerical integration of eqn. (42) through the commercial code MATLAB by exploiting the continuation toolbox MATCONT [55] (employing ode45 solver, {Relative Tolerance, Absolute Tolerance, Initial Time Step}  $\approx 10^{-8}$  and Maximum Time Step  $\approx 10^{-4}$ ). Considering the inherent non-smoothness of the equation of motion (42) and the prerequisites for using the continuation toolbox, a necessary adjustment is introduced to smoothen the sign function  $\text{sgn}[\theta(\tau)]$  by approximating it through the following exponential function  $q(\theta(\tau), \mathcal{B})$

$$q(\theta(\tau), \mathcal{B}) = \frac{e^{\mathcal{B}\theta(\tau)} - 1}{e^{\mathcal{B}\theta(\tau)} + 1}, \quad (89)$$

by considering large values of the dimensionless quantity  $\mathcal{B}$ , selected to not compromise the accuracy of the limit cycle while the continuation method converges. To verify the accuracy of the model and selected parameter  $\mathcal{B}$ , the parts corresponding to stable motions of the MATCONT outputs have been independently confirmed

through a direct integration of the non-smooth equation of motion in MATLAB (without any smoothing of the  $\text{sgn}$  function) by means of the same solver and options adopted in the continuation method.

By introducing  $\theta_{\text{st}}$  as the difference angle corresponding to the quasi-static equilibrium under the loads  $\mathcal{H} = \hat{\mathcal{H}}$  and  $\mathcal{V} = \bar{\mathcal{V}}$  when the system is harmonically loaded and  $\theta_{\text{eq}}$  as the equivalent rotation angle when the system is under an harmonic ground motion with amplitude  $\hat{\zeta}$

$$\theta_{\text{eq}} = \arccos(\cos \beta_0 - \hat{\zeta}) - \beta_0, \quad (90)$$

the dynamic response is reported in terms of dimensionless rotation  $\max_{\tau} |\theta(\tau)| / \theta_{\text{st}}$  or  $\max_{\tau} |\theta(\tau)| / \theta_{\text{eq}}$ . As graphical convention, the sets of stable configuration are drawn with a continuous blue line while the unstable ones with a dashed red line; frequency range displaying quasi-periodic (QP) and chaotic (CH) responses are highlighted through light blue and light orange bands, respectively. Moreover, in some of the reported spectra, a horizontal dashed green line appears at the difference angle  $\bar{\theta}^{[1]} = \pi - \beta_0 = 110^\circ$ , corresponding to the smallest rotation for which the layer of parallelogram shape reduces into a straight line.

The response spectra under the loading condition (i), eqn. (86), are reported in Fig. 9 with varying the angular frequency  $\Omega$  for different horizontal load amplitudes  $\hat{\mathcal{H}} = \{0.2, 0.5, 1, 1.5, 2, 3\}$ . It can be noted that:

- for sufficiently small load amplitudes ( $\hat{\mathcal{H}} = 0.2$ ) a classical frequency response curve for the primary resonance is qualitatively detected, which is modified through the emergence of some unstable branches and loops (knots) when the load amplitude increases ( $\hat{\mathcal{H}} = \{0.5, 1, 1.5\}$ ). Remarkably, the self-intersection appearing when a portion of spectrum displays a knot shape is related to two different stable dynamic steady states with the same amplitude and frequency but shifted in their phase;
- super-harmonic resonances are displayed, also with some unstable branches (see the zoom-in frames for  $\hat{\mathcal{H}} = \{0.2, 0.5\}$ , but also for higher  $\hat{\mathcal{H}}$ ) and lead to quasi-periodic motions ( $\hat{\mathcal{H}} = 0.2$ );
- for sufficiently large load amplitudes ( $\hat{\mathcal{H}} = \{0.5, 1, 1.5, 2, 3\}$ ), a portion of spectrum appears as a loop detached from the main one defining larger rotation amplitudes and where, due to the loop shape, the jump-phenomena occur at the saddle node equilibria;
- a region of chaotic response appears for large load amplitudes ( $\hat{\mathcal{H}} = \{2, 3\}$ ) for a range of frequencies becoming wider with the increase of  $\hat{\mathcal{H}}$ . This can be interpreted as the collision of the coexisting equilibria, occurring approximately within the frequency range  $\Omega \in [1, 2]$ . Interestingly, the system may display the well-known *grazing* phenomenon [56, 57, 58, 59, 60, 61, 62], for which a stable path can pass through a chaotic region ( $\hat{\mathcal{H}} = 3$ ).

The response spectra under the loading condition (ii.), eqn. (87), are reported in Fig. 10 with varying angular frequency  $\Omega$  and for different ground motion amplitudes  $\hat{\zeta} = \{0.25, 0.5\}$ . It can be observed that:

- differently from the loading condition (i.), super-harmonic resonances are no longer present, while detached portions of spectrum still appear;
- quasi-periodic response may occur at low frequencies as transition zone between the undeformed state and the steady state ( $\hat{\zeta} = 0.5$ ), as the amplitude of the ground motion increases;
- chaotic response is also detected for high frequencies as  $\hat{\zeta}$  increases.

To further assess the dynamic response and the existence of stable attractors, bifurcation diagrams have been obtained under the loading conditions (i) and (iii) as maximum absolute value of rotation  $\max_{\tau} |\theta(\tau)|$  with varying the horizontal load amplitude  $\hat{\mathcal{H}}$  for different values of frequency  $\Omega$ . In particular, the bifurcation diagrams for the loading condition (i) are reported in Fig. 11, for  $\Omega = \{0.5, 1\}$  and in Fig. 12, for  $\Omega = \{2, 4\}$ . The purple vertical dashed line represents the quasi-static bifurcation condition (QSB), defined by  $\hat{\mathcal{H}}_{\text{cr}}^{\text{QS}} = |\bar{\mathcal{V}} / \tan \beta_0|$ . It can be observed that:



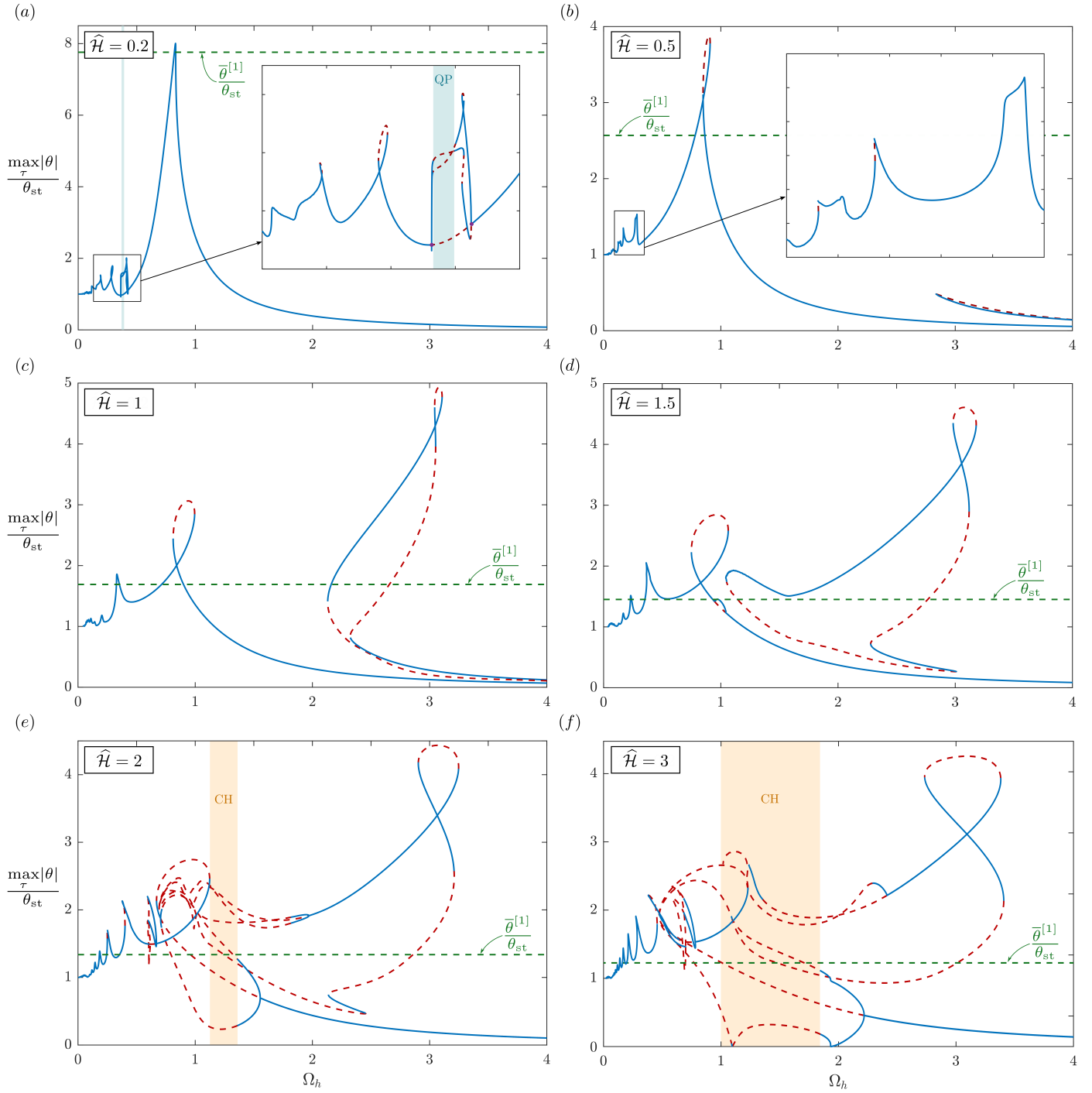


Figure 9: Normalized maximum absolute value of the difference angle  $\theta$  - frequency  $\Omega$  response spectrum for the system with  $\beta_0 = 80^\circ$  and  $\mathcal{C} = 0.1$  under loading condition (i), eqn. (86), corresponding to harmonic horizontal load  $\mathcal{H}(\tau) = \hat{\mathcal{H}} \sin(\Omega\tau)$  with amplitude  $\hat{\mathcal{H}} = \{0.2, 0.5, 1, 1.5, 2, 3\}$  at constant vertical loading  $\bar{\mathcal{V}} = -0.5$ . The stable (unstable) configurations are represented as continuous (dashed) blue (red) line on the spectrum. The dashed horizontal green line represents the smallest difference angle  $\theta$  for which the parallelogram reduces into a straight line, while the light blue band represents a quasi periodic (QP) response and the light orange band a chaotic (CH) response.

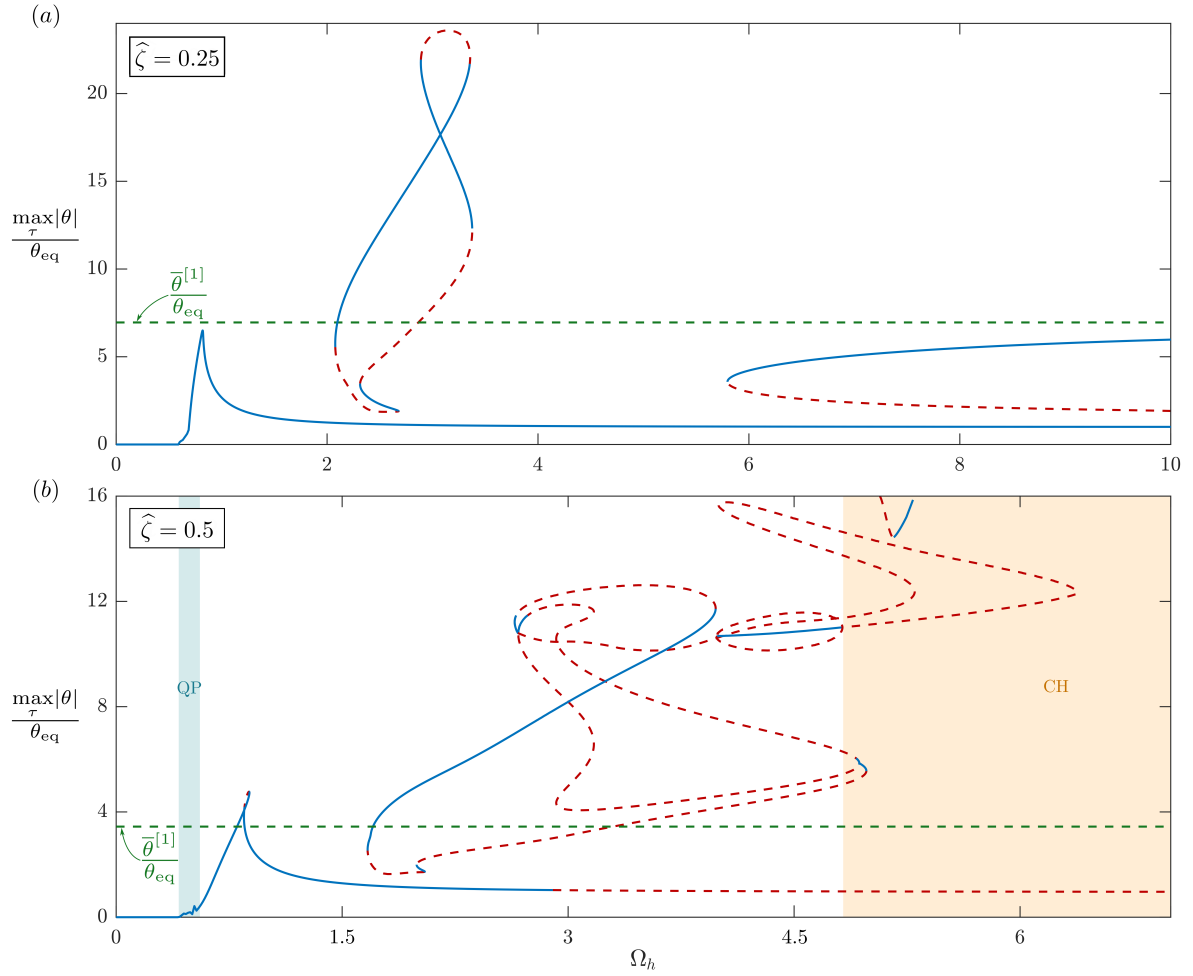


Figure 10: As for Fig. 9, but under loading condition (ii), eqn. (87), corresponding to harmonic horizontal ground motion  $\zeta(\tau) = \hat{\zeta} \sin(\Omega\tau)$  with amplitude (a)  $\hat{\zeta} = \{0.25, 0.5\}$  at constant vertical loading  $\bar{V} = -0.5$ .

- the undeformed state ( $\theta = 0$ ) becomes unstable for  $\hat{\mathcal{H}} > \hat{\mathcal{H}}_{cr}^{QS}$ . Moreover, a supercritical (stable) limit-cycle exists for  $\hat{\mathcal{H}} < \hat{\mathcal{H}}_{cr}^{QS}$  with varying the frequency  $\Omega$ , providing an anticipation of the bistable response within the quasi-static monostability domain due to dynamics effects (this feature is further analyzed later);
- the amplitude of the first limit-cycle increases with  $\hat{\mathcal{H}}$  and, for a given  $\hat{\mathcal{H}}$ , decreases with  $\Omega$ , i.e. a flattening of first bifurcated paths manifests itself as the frequency of excitation increases;
- for sufficiently large  $\hat{\mathcal{H}}$  a very complex dynamic behavior can be detected for which grazing together with a cascade of period doubling bifurcations occur, which constitutes the route for a chaotic response;
- the chaotic response appears for two disconnected sets of load amplitudes  $\hat{\mathcal{H}}$ . Indeed, large-amplitude stable steady states exist between the two chaotic regions, bifurcating through period doubling cascade and also grazing [56, 57, 58, 59, 60, 61, 62] in chaos (see Figs. 11-a,b);
- an increase of the frequency  $\Omega$  shifts the region where chaos occurs to larger values of load amplitude  $\hat{\mathcal{H}}$ ;
- the coexistence of multiple stable attractors is analogous to what observed in the response spectra. More specifically, the number of stable attractors increases with the increase of the horizontal load amplitude  $\hat{\mathcal{H}}$ . Moreover, the piercing of a stable attractor within a chaotic region (Fig. 11-b) corresponds to the

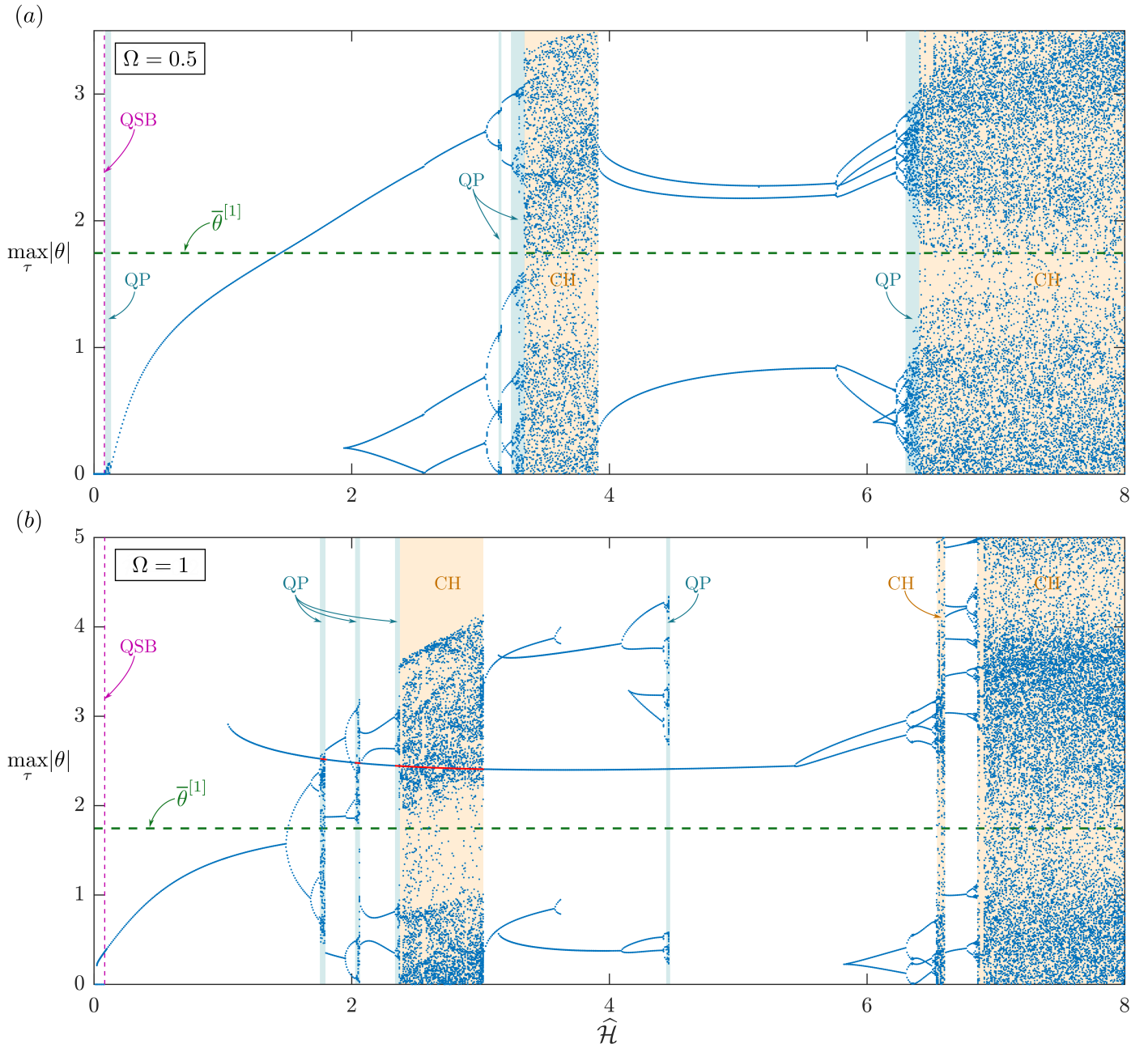


Figure 11: Maximum absolute value of the difference angle  $\theta$  - horizontal load amplitude  $\hat{\mathcal{H}}$  bifurcation diagram for the system with  $\beta_0 = 80^\circ$  and  $\mathcal{C} = 0.1$  under loading condition (i), eqn. (86), corresponding to constant vertical loading  $\bar{\mathcal{V}} = -0.5$  and harmonic horizontal loading  $\mathcal{H}(\tau) = \hat{\mathcal{H}} \sin(\Omega\tau)$  and frequency  $\Omega = \{0.5, 1\}$ .

presence of stable configuration within the range of frequencies providing chaos (light orange band) in the spectra of Figs. 9-f and 10-b.

While the behaviour is symmetric under loading conditions (i) and (ii), the dynamic response is no longer symmetric under loading condition (iii), (88), since it is related to an elliptical loading path in the  $\mathcal{H} - \mathcal{V}$  plane (Fig. 8-b), therefore sensitive to the direction. Such non-symmetric behavior can be appreciated from the bifurcation diagram reported in terms of maximum and minimum values of rotation,  $\max_{\tau} \{\theta(\tau)\}$  and  $\min_{\tau} \{\theta(\tau)\}$ , in Fig. 13 for  $\bar{\mathcal{V}} = -0.5$ ,  $\hat{\mathcal{V}} = 0.25$ , and  $\Omega = 1$ . However, apart for the lack of symmetry, the

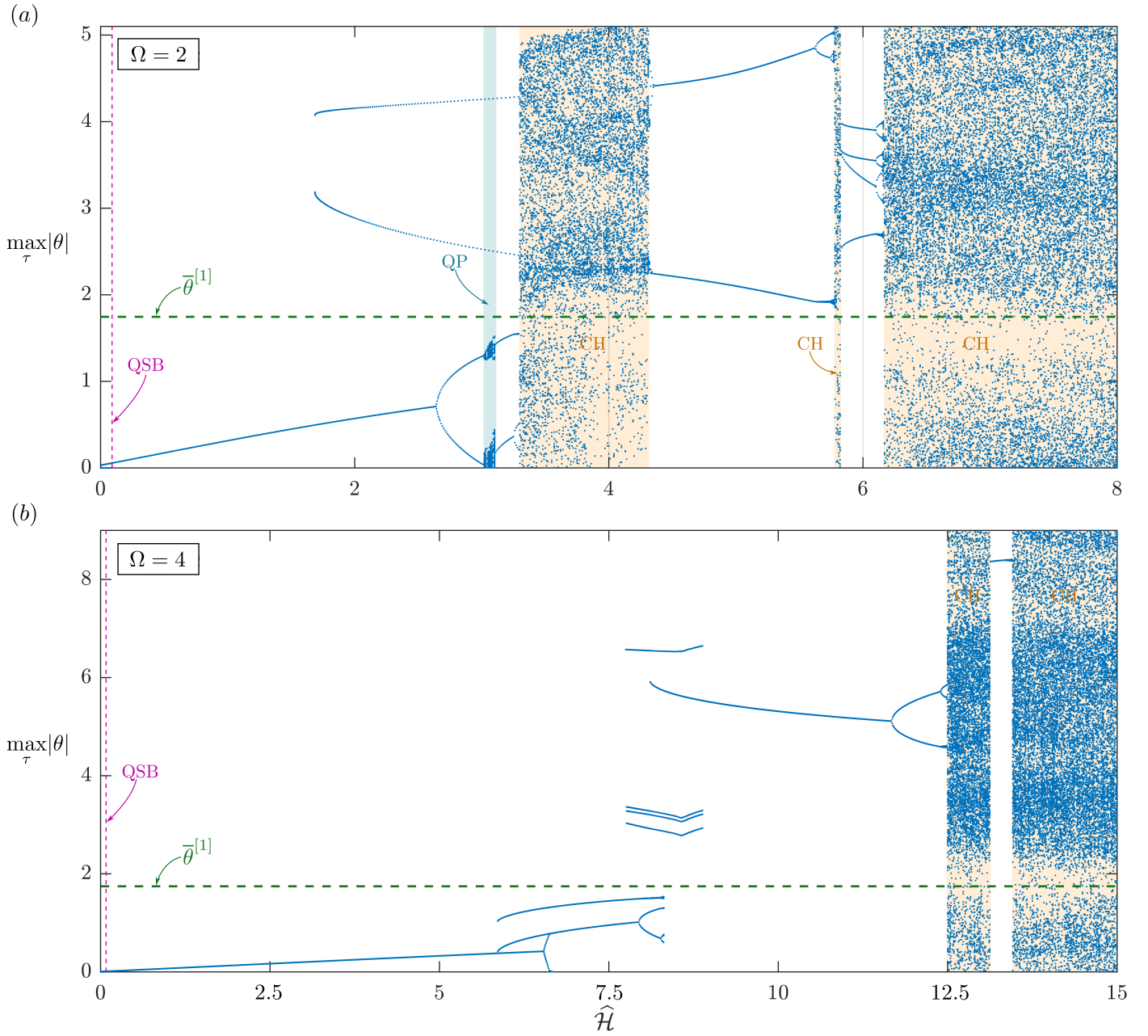


Figure 12: As for Fig. 11, but for horizontal force frequencies  $\Omega = \{2, 4\}$ .

same features and the coexistence of multiple equilibrium paths observed in the symmetric response are also detected here.

A final investigation on the dynamic behaviour is addressed in terms of the largest rotation amplitude among the non-trivial solutions under loading condition (i), eqn. (86). The results are reported through stability charts in Figs. 14 and 15, realized as contourplots in the  $(\hat{\mathcal{H}}, \bar{\mathcal{V}})$  plane. White and coloured regions represent respectively the non-existence and existence of non-trivial stable configurations for the corresponding loading pairs  $(\hat{\mathcal{H}}, \bar{\mathcal{V}})$ , with the contours associated with the rotation amplitude of the non-trivial stable solution. Since under quasi-static loading conditions non-trivial equilibrium configurations exist only when  $\mathcal{V} \cos \beta_0 > -|\mathcal{H}| \sin \beta_0$  (red line), it can be appreciated that dynamics reduces the monostability region by increasing

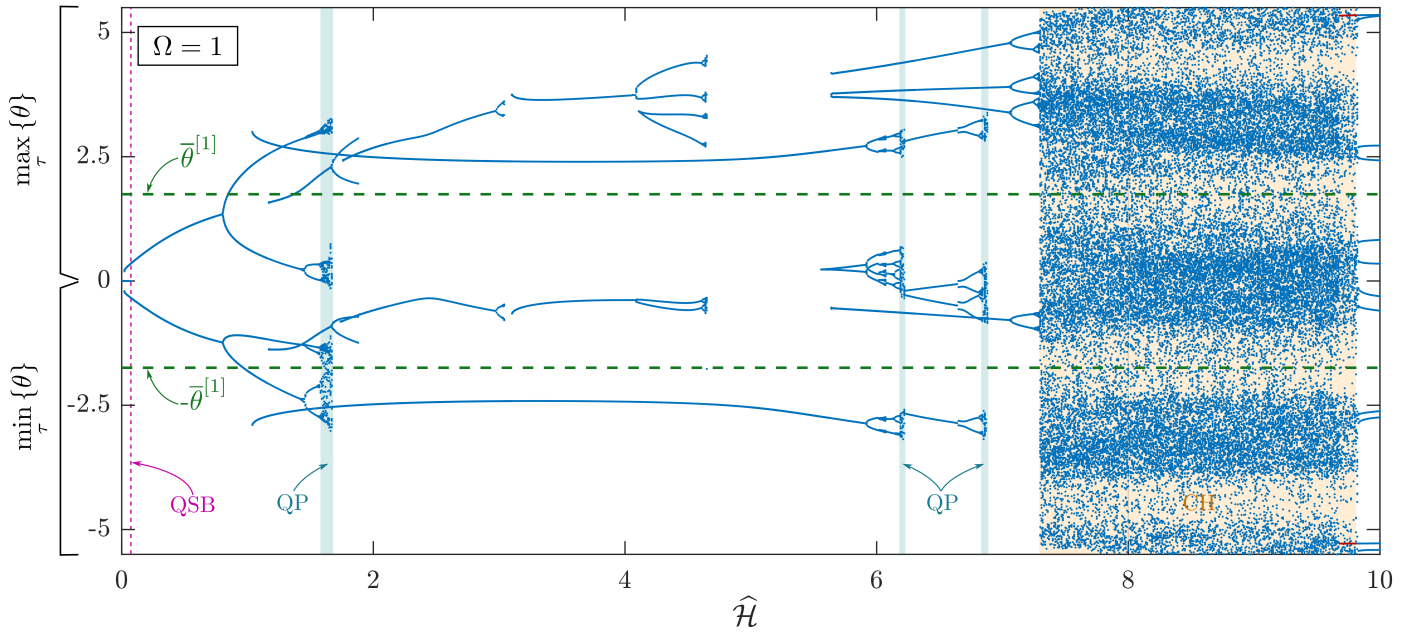


Figure 13: As for Fig. 11, but under loading condition (iii), eqn. (88), corresponding to harmonic horizontal and vertical forces ( $\mathcal{H}(\tau) = \hat{\mathcal{H}} \sin(\Omega\tau)$ ,  $\mathcal{V}(\tau) = \bar{\mathcal{V}} + \hat{\mathcal{V}} \cos(\Omega\tau)$ ) with frequency  $\Omega = 1$ , vertical force average  $\bar{\mathcal{V}} = -0.5$  and amplitude  $\hat{\mathcal{V}} = 0.25$ , with varying amplitude of the horizontal force  $\hat{\mathcal{H}}$ . Since the loading is no longer symmetric, the system response loses symmetry and therefore maximum and minimum rotations are reported separately.

the multistability one, therefore realizing an enlargement of the co-existence domain for the stable trivial and non-trivial solutions. In particular, the stability charts reported in Fig. 14 for different frequencies,  $\Omega = \{0.1, 0.5, 0.75, 1, 1.5, 4\}$ , show that the multistability region increases more with the increase of the excitation frequency  $\Omega$ , while the corresponding amplitudes reach instead highest values for  $\Omega \approx 1$ . It is also noted that a second non-trivial stable motion appears for a narrow region in the load values  $(\hat{\mathcal{H}}, \bar{\mathcal{V}})$  when  $\Omega = 4$ .

The influence of the initial configuration angle  $\beta_0$  and of the damping coefficient  $\mathcal{C}$  can be appreciated from the stability charts for  $\beta_0 = 60^\circ$  and  $\mathcal{C} = 0.1$  (Fig.15-a), for  $\beta_0 = 80^\circ$  and  $\mathcal{C} = 0.05$  (Fig.15-b), and for  $\beta_0 = 80^\circ$  and  $\mathcal{C} = 0.15$  (Fig.15-c), all of these for an horizontal load frequency  $\Omega = 1$ . It is noted that the initial configuration angle  $\beta_0$  has only a slight influence on the shape of the new border (compare Figs. 14-d) and Fig.15-a)), although the maximum amplitude decreases with the increase of  $\beta_0$ . Moreover, the lower the damping coefficient  $\mathcal{C}$ , the more the domain of non-trivial solutions extends, as well as the higher the damping coefficient  $\mathcal{C}$ , the lower the maximum rotation amplitude of the non-trivial solution.

It is worth to remark that the external load also entails a parametric excitation through a change in the equivalent stiffness in the equation of motion (53). Therefore, the reported stability charts resembles in a sense a sort of Strutt-like diagram, although an interplay between the external and the parametric excitation occurs in the present system, differently from the classical Mathieu problem.

## 7 Conclusions

The nonlinear dynamic response has been investigated for a novel metainterface based on two layers of elements buckling in tension (or equivalently in compression) modeled as a two degree of freedom system, where each degree is subject to a unilateral constraint. A system of two nonlinear coupled equations of motion under unilateral constraints have been obtained and, by assuming no bouncing at impact among all the possible impact scenarios, reduced to a single nonlinear piecewise-smooth equation of motion, resembling that governing



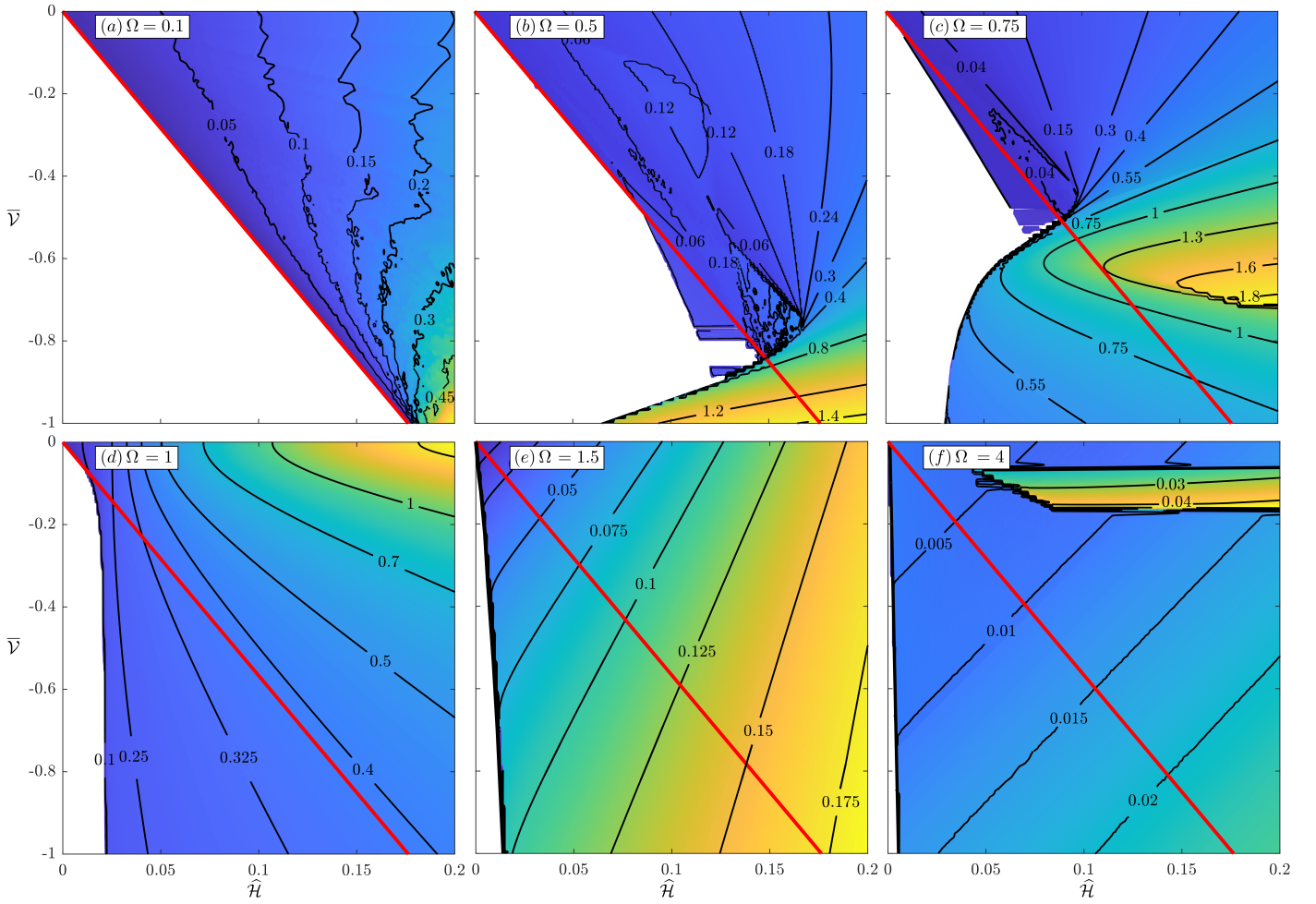


Figure 14: Dynamic stability chart for the system with  $\beta_0 = 80^\circ$  and  $\mathcal{C} = 0.1$  under loading condition (i), eqn. (86), corresponding to harmonic horizontal loading  $\mathcal{H}(\tau) = \hat{\mathcal{H}} \sin(\Omega\tau)$  with varying frequency  $\Omega = \{0.1, 0.5, 0.75, 1, 1.5, 4\}$  at constant vertical loading  $\bar{\mathcal{V}}$ . White area represents the monostable region where only the trivial configuration is stable, while the colored region represents the presence of at least one non-trivial stable configuration. The border of the monostable region under quasi-static conditions is drawn as the red line, showing that dynamics anticipates the bistability. Contour levels display the largest rotation amplitude  $\theta_{\max}$  of the non-trivial stable solutions.

the rocking oscillations of rigid blocks. Vibrations are then investigated under constant loadings, disclosing divergence condition for small amplitude vibrations, the phase portraits at large amplitude vibrations, and the possibility to realize a bouncing-like motion from a no-bouncing system with extreme stiffness ratios. Finally, vibration analysis is extended to oscillatory loadings through the presentation of response spectra, bifurcation diagrams, and stability charts, which show a wide landscape of the metainterface response, encompassing dynamic bifurcations and multistability anticipation.

The disclosure of such interesting features within a theoretical framework asks now for an experimental validation and a tuning of dissipation parameters towards an effective implementation of the present metainterface concept in engineering applications ranging from energy harvesting to vibration mitigation.



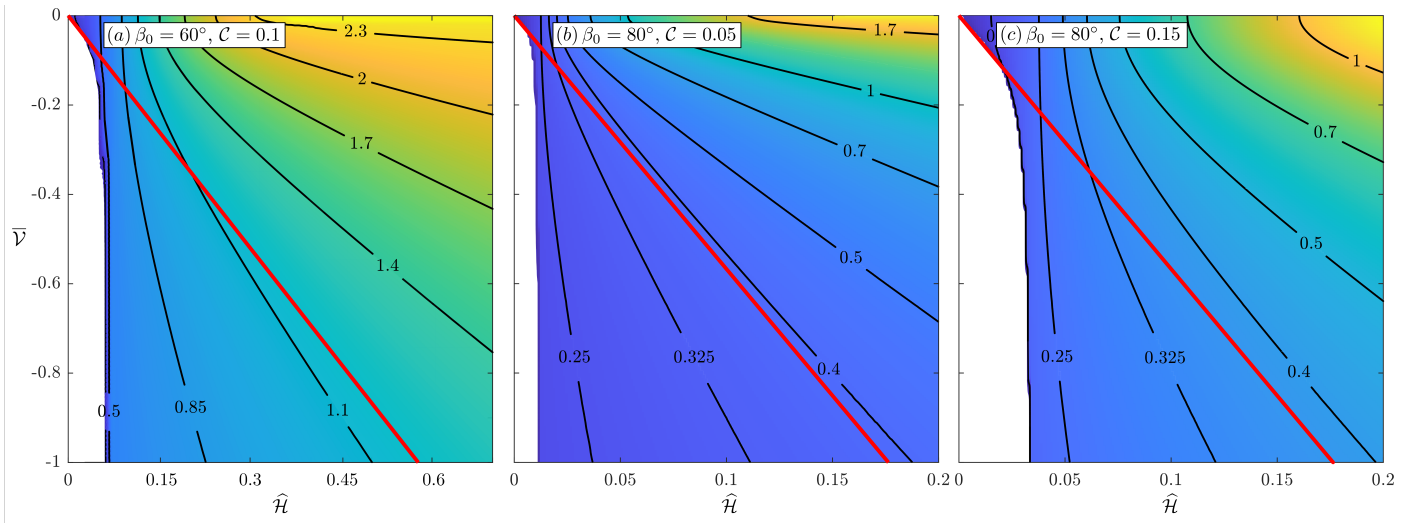


Figure 15: As for Fig. 14, but for a system with a)  $\beta_0 = 60^\circ$  and  $\mathcal{C} = 0.1$ , b)  $\beta_0 = 80^\circ$  and  $\mathcal{C} = 0.05$ , and c)  $\beta_0 = 80^\circ$  and  $\mathcal{C} = 0.15$ , with an horizontal load frequency  $\Omega = 1$ .

## Acknowledgements

NH gratefully acknowledges the financial support from the European Union's Horizon 2020 research and innovation programme under the Marie Skłodowska-Curie grant agreement 'INSPIRE - Innovative ground interface concepts for structure protection' PITN-GA-2019-813424-INSPIRE. FDC and FDA gratefully acknowledge financial support from the ERC advanced grant ERC-ADG-2021-101052956-BEYOND. Support from the Italian Ministry of Education, University and Research (MIUR) in the frame of the 'Departments of Excellence' grant L. 232/2016 is acknowledged. This work has been developed under the auspices of INDAM-GNFM.

## References

- [1] D. M. Kochmann and K. Bertoldi, "Exploiting Microstructural Instabilities in Solids and Structures: From Metamaterials to Structural Transitions," *Applied Mechanics Reviews*, vol. 69, 10 2017. 050801.
- [2] C.-M. Lee and V. Goverdovskiy, "A multi-stage high-speed railroad vibration isolation system with "negative" stiffness," *Journal of Sound and Vibration*, vol. 331, no. 4, pp. 914–921, 2012.
- [3] H. W. Yap, R. S. Lakes, and R. W. Carpick, "Negative stiffness and enhanced damping of individual multiwalled carbon nanotubes," *Phys. Rev. B*, vol. 77, p. 045423, Jan 2008.
- [4] H. Ma, K. Wang, H. Zhao, R. Mu, and B. Yan, "A reusable metastructure for tri-directional energy dissipation," *International Journal of Mechanical Sciences*, vol. 214, p. 106870, 2022.
- [5] H. Ma, K. Wang, H. Zhao, W. Shi, J. Xue, Y. Zhou, Q. Li, G. Wang, and B. Yan, "Energy dissipation and shock isolation using novel metamaterials," *International Journal of Mechanical Sciences*, vol. 228, p. 107464, 2022.
- [6] P. Wang, F. Casadei, S. Shan, J. C. Weaver, and K. Bertoldi, "Harnessing buckling to design tunable locally resonant acoustic metamaterials," *Phys. Rev. Lett.*, vol. 113, p. 014301, Jul 2014.
- [7] X. Guo, V. E. Gusev, K. Bertoldi, and V. Tournat, "Manipulating acoustic wave reflection by a nonlinear elastic metasurface," *J. Appl. Phys.*, vol. 123, p. 124901, mar 2018.

- 
- [8] F. Xin and T. Lu, “Tensional acoustomechanical soft metamaterials,” *Sci. Rep.*, vol. 6, p. 27432, jun 2016.
- [9] J. T. B. Overvelde, S. Shan, and K. Bertoldi, “Compaction through buckling in 2d periodic, soft and porous structures: Effect of pore shape,” *Advanced Materials*, vol. 24, no. 17, pp. 2337–2342, 2012.
- [10] D. Melancon, A. E. Forte, L. M. Kamp, B. Gorissen, and K. Bertoldi, “Inflatable origami: Multimodal deformation via multistability,” *Advanced Functional Materials*, vol. 32, no. 35, p. 2201891, 2022.
- [11] K. Liu, P. P. Pratapa, D. Misseroni, T. Tachi, and G. H. Paulino, “Triclinic metamaterials by tristable origami with reprogrammable frustration,” *Advanced Materials*, vol. 34, no. 43, p. 2107998, 2022.
- [12] T. Chen, O. R. Bilal, K. Shea, and C. Daraio, “Harnessing bistability for directional propulsion of soft, untethered robots,” *Proceedings of the National Academy of Sciences*, vol. 115, no. 22, pp. 5698–5702, 2018.
- [13] W.-K. Lee, D. J. Preston, M. P. Nemitz, A. Nagarkar, A. K. MacKeith, B. Gorissen, N. Vasios, V. Sanchez, K. Bertoldi, L. Mahadevan, and G. M. Whitesides, “A buckling-sheet ring oscillator for electronics-free, multimodal locomotion,” *Science Robotics*, vol. 7, no. 63, p. eabg5812, 2022.
- [14] D. Zaccaria, D. Bigoni, G. Noselli, and D. Misseroni, “Structures buckling under tensile dead load,” *Proc. R. Soc. A Math. Phys. Eng. Sci.*, vol. 467, pp. 1686–1700, jun 2011.
- [15] S. Palumbo, A. R. Carotenuto, A. Cutolo, D. R. Owen, L. Deseri, and M. Fraldi, “Bulky auxeticity, tensile buckling and deck-of-cards kinematics emerging from structured continua,” *Proceedings of the Royal Society A: Mathematical, Physical and Engineering Sciences*, vol. 477, no. 2246, p. 20200729, 2021.
- [16] F. Bosi, D. Misseroni, F. Dal Corso, S. Neukirch, and D. Bigoni, “Asymptotic self-restabilization of a continuous elastic structure,” *Phys. Rev. E*, vol. 94, p. 063005, Dec 2016.
- [17] D. Bigoni, F. Bosi, F. Dal Corso, and D. Misseroni, “Instability of a penetrating blade,” *Journal of the Mechanics and Physics of Solids*, vol. 64, pp. 411–425, 2014.
- [18] P. Koutsogiannakis, D. Bigoni, and F. Dal Corso, “Double restabilization and design of force–displacement response of the extensible elastica with movable constraints,” *European Journal of Mechanics - A/Solids*, p. 104745, 2022.
- [19] C. Fu, T. Wang, F. Xu, Y. Huo, and M. Potier-Ferry, “A modeling and resolution framework for wrinkling in hyperelastic sheets at finite membrane strain,” *Journal of the Mechanics and Physics of Solids*, vol. 124, pp. 446–470, 2019.
- [20] Q. Li and T. J. Healey, “Stability boundaries for wrinkling in highly stretched elastic sheets,” *Journal of the Mechanics and Physics of Solids*, vol. 97, pp. 260–274, 2016. SI: Pierre Suquet Symposium.
- [21] M. Taylor, K. Bertoldi, and D. J. Steigmann, “Spatial resolution of wrinkle patterns in thin elastic sheets at finite strain,” *Journal of the Mechanics and Physics of Solids*, vol. 62, pp. 163–180, 2014.
- [22] A. Cazzolli, F. Dal Corso, and D. Bigoni, “Flutter Instability and Ziegler Destabilization Paradox for Elastic Rods Subject to Non-Holonomic Constraints,” *Journal of Applied Mechanics*, vol. 88, 12 2020. 031003.
- [23] A. Cazzolli, F. Dal Corso, and D. Bigoni, “Non-holonomic constraints inducing flutter instability in structures under conservative loadings,” *Journal of the Mechanics and Physics of Solids*, vol. 138, p. 103919, 2020.

- 
- [24] A. Fargette, S. Neukirch, and A. Antkowiak, “Elastocapillary Snapping: Capillarity Induces Snap-Through Instabilities in Small Elastic Beams,” *Physical Review Letters*, vol. 112, p. 137802, Apr. 2014.
- [25] P. Grandgeorge, A. Antkowiak, and S. Neukirch, “Auxiliary soft beam for the amplification of the elastocapillary coiling: Towards stretchable electronics,” *Advances in Colloid and Interface Science*, vol. 255, pp. 2–9, 2018.
- [26] P. Grandgeorge, N. Krins, A. Hourlier-Fargette, C. Laberty-Robert, S. Neukirch, and A. Antkowiak, “Capillarity-induced folds fuel extreme shape changes in thin wicked membranes,” *Science*, vol. 360, no. 6386, pp. 296–299, 2018.
- [27] F. Xu, S. Zhao, C. Lu, and M. Potier-Ferry, “Pattern selection in core-shell spheres,” *Journal of the Mechanics and Physics of Solids*, vol. 137, p. 103892, 2020.
- [28] F. Xu, Y. Huang, S. Zhao, and X.-Q. Feng, “Chiral topographic instability in shrinking spheres,” *Nat. Comput. Sci.*, vol. 2, no. 10, pp. 632–640, 2022.
- [29] E. Siéfert, E. Reyssat, J. Bico, and B. Roman, “Bio-inspired pneumatic shape-morphing elastomers,” *Nature materials*, vol. 18(1), pp. 24–28, 2014.
- [30] E. Barchiesi, M. Spagnuolo, and L. Placidi, “Mechanical metamaterials: a state of the art,” *Mathematics and Mechanics of Solids*, vol. 24, no. 1, pp. 212–234, 2019.
- [31] N. I. Zheludev and Y. S. Kivshar, “From metamaterials to metadevices,” *Nat. Mater.*, vol. 11, no. 11, pp. 917–924, 2012.
- [32] X. Zhao, G. Duan, A. Li, C. Chen, and X. Zhang, “Integrating microsystems with metamaterials towards metadevices,” *Microsystems Nanoeng.*, vol. 5, no. 1, p. 5, 2019.
- [33] J. Z. Kim, Z. Lu, A. S. Blevins, and D. S. Bassett, “Nonlinear dynamics and chaos in conformational changes of mechanical metamaterials,” *Phys. Rev. X*, vol. 12, p. 011042, Mar 2022.
- [34] F. D’Annibale, G. Rosi, and A. Luongo, “Piezoelectric control of hopf bifurcations: A non-linear discrete case study,” *International Journal of Non-Linear Mechanics*, vol. 80, pp. 160–169, 2016. Dynamics, Stability, and Control of Flexible Structures.
- [35] F. D’Annibale, “Piezoelectric control of the Hopf bifurcation of Ziegler’s column with nonlinear damping,” *Nonlinear Dyn.*, vol. 86, no. 4, pp. 2179–2192, 2016.
- [36] N. S. Saravana Jothi and A. Hunt, “Active mechanical metamaterial with embedded piezoelectric actuation,” *APL Materials*, vol. 10, no. 9, p. 091117, 2022.
- [37] V. Settimi, M. Lepidi, and A. Bacigalupo, “Nonlinear dispersion properties of one-dimensional mechanical metamaterials with inertia amplification,” *International Journal of Mechanical Sciences*, vol. 201, p. 106461, 2021.
- [38] N. Hima, D. Bigoni, and F. Dal Corso, “Buckling versus unilateral constraint for a multistable metamaterial element,” *Philosophical Transactions of the Royal Society A: Mathematical, Physical and Engineering Sciences*, vol. 380, no. 2231, p. 20220021, 2022.
- [39] D. J. W. Simpson, *Bifurcations in Piecewise-Smooth Continuous Systems*. WORLD SCIENTIFIC, 2010.
- [40] Y. Zhang and Q. Cao, “The recent advances for an archetypal smooth and discontinuous oscillator,” *International Journal of Mechanical Sciences*, vol. 214, p. 106904, 2022.

- [41] L. Charroyer, O. Chiello, and J.-J. Sinou, “Self-excited vibrations of a non-smooth contact dynamical system with planar friction based on the shooting method,” *International Journal of Mechanical Sciences*, vol. 144, pp. 90–101, 2018.
- [42] G. W. Housner, “The behavior of inverted pendulum structures during earthquakes,” *Bull. Seismol. Soc. Am.*, vol. 53, pp. 403–417, feb 1963.
- [43] G. Augusti and A. Sinopoli, “Modelling the Dynamics of Large Block Structures,” *Meccanica*, vol. 27, pp. 195–211, sep 1992.
- [44] C.-S. Yim, A. K. Chopra, and J. Penzien, “Rocking response of rigid blocks to earthquakes,” *Earthq. Eng. Struct. Dyn.*, vol. 8, pp. 565–587, jan 1980.
- [45] R. H. Plaut, W. T. Fielder, and L. N. Virgin, “Fractal behavior of an asymmetric rigid block overturning due to harmonic motion of a tilted foundation,” *Chaos, Solitons & Fractals*, vol. 7, no. 2, pp. 177–196, 1996.
- [46] N. Makris and Y. Roussos, “Rocking Response of Rigid Blocks Under Near-Source Motions,” *Geotechnique*, vol. 50, may 1999.
- [47] Z. Jian and M. Nicos, “Rocking Response of Free-Standing Blocks under Cycloidal Pulses,” *J. Eng. Mech.*, vol. 127, pp. 473–483, may 2001.
- [48] F. Masi, I. Stefanou, P. Vannucci, and V. Maffi-Berthier, “Rocking response of inverted pendulum structures under blast loading,” *International Journal of Mechanical Sciences*, vol. 157-158, pp. 833–848, 2019.
- [49] S. J. Hogan and T. B. Benjamin, “On the dynamics of rigid-block motion under harmonic forcing,” *Proceedings of the Royal Society of London. A. Mathematical and Physical Sciences*, vol. 425, no. 1869, pp. 441–476, 1989.
- [50] E. G. Dimitrakopoulos and M. J. DeJong, “Revisiting the rocking block: closed-form solutions and similarity laws,” *Proc. R. Soc. A Math. Phys. Eng. Sci.*, vol. 468, pp. 2294–2318, aug 2012.
- [51] A. Kounadis, “Parametric study in rocking instability of a rigid block under harmonic ground pulse: A unified approach,” *Soil Dyn. Earthq. Eng.*, vol. 45, pp. 125–143, feb 2013.
- [52] M. F. Vassiliou, R. Truniger, and B. Stojadinović, “An analytical model of a deformable cantilever structure rocking on a rigid surface: development and verification,” *Earthq. Eng. Struct. Dyn.*, vol. 44, pp. 2775–2794, dec 2015.
- [53] J. A. Bachmann, M. Strand, M. F. Vassiliou, M. Broccardo, and B. Stojadinović, “Is rocking motion predictable?,” *Earthq. Eng. Struct. Dyn.*, vol. 47, pp. 535–552, feb 2018.
- [54] M. F. Vassiliou, M. Broccardo, C. Cengiz, M. Dietz, L. Dihoru, S. Gunay, K. M. Mosalam, G. Mylonakis, A. Sextos, and B. Stojadinovic, “Shake table testing of a rocking podium: Results of a blind prediction contest,” *Earthq. Eng. Struct. Dyn.*, vol. 50, pp. 1043–1062, apr 2020.
- [55] A. Dhooge, W. Govaerts, and Y. A. Kuznetsov, “Matcont: A matlab package for numerical bifurcation analysis of odes,” *ACM Trans. Math. Softw.*, vol. 29, p. 141–164, jun 2003.
- [56] G. Wen, S. Yin, H. Xu, S. Zhang, and Z. Lv, “Analysis of grazing bifurcation from periodic motion to quasi-periodic motion in impact-damper systems,” *Chaos, Solitons & Fractals*, vol. 83, pp. 112–118, 2016.
- [57] J. Thompson and R. Ghaffari, “Chaos after period-doubling bifurcations in the resonance of an impact oscillator,” *Physics Letters A*, vol. 91, no. 1, pp. 5–8, 1982.

- [58] W. Chin, E. Ott, H. E. Nusse, and C. Grebogi, “Grazing bifurcations in impact oscillators,” *Phys. Rev. E*, vol. 50, pp. 4427–4444, Dec 1994.
- [59] C. Budd, F. Dux, and A. Cliffe, “The effect of frequency and clearance variations on single-degree-of-freedom impact oscillators,” *Journal of Sound and Vibration*, vol. 184, no. 3, pp. 475–502, 1995.
- [60] X. Lyu, Q. Gao, and G. Luo, “Dynamic characteristics of a mechanical impact oscillator with a clearance,” *International Journal of Mechanical Sciences*, vol. 178, p. 105605, 2020.
- [61] H. Jiang, A. S. Chong, Y. Ueda, and M. Wiercigroch, “Grazing-induced bifurcations in impact oscillators with elastic and rigid constraints,” *International Journal of Mechanical Sciences*, vol. 127, pp. 204–214, 2017. Special Issue from International Conference on Engineering Vibration - ICoEV 2015.
- [62] S. Yin, J. Ji, and G. Wen, “Complex near-grazing dynamics in impact oscillators,” *International Journal of Mechanical Sciences*, vol. 156, pp. 106–122, 2019.

## A Rocking motion of a rigid rectangular block over an oscillating rigid flat surface

The rocking motion of a rigid rectangular body has strong similarities with the dynamics of the structural system presented in the main text, including a previously undisclosed condition providing energy increase at impact.

The kinetic energy  $\mathcal{T}(t)$  of a rigid rectangular block over an rigid flat surface, oscillating through a displacement  $U_h(t) = 4R\zeta(t)/3$ , is given by

$$\mathcal{T}(t) = \frac{2MR^2}{3} \left( \dot{\theta}(t)^2 + 4\dot{\zeta}(t)^2 + 2\dot{\theta}(t)\dot{\zeta}(t) \cos(\alpha - |\theta(t)|) \right), \quad (91)$$

where  $M$  is the mass of the rigid block,  $\alpha$  is the angle between the radius  $R$  connecting the center of the mass of the body to its pivoting point and the vertical direction when the block is at rest, and  $\theta(t)$  is the rotation of the rectangular body around the pivoting point.

Since the potential energy  $\Pi(t)$  is given as the gravitational potential of the block due to the gravity acceleration  $g$  as

$$\Pi(t) = MgR [\cos(\alpha - |\theta(t)|) - \cos \alpha], \quad (92)$$

the Euler-Lagrange equation leads to the celebrated nonlinear equation of rocking motion derived for the first time by Housner [42]

$$\ddot{\theta}(t) = -\ddot{\zeta}(t) \cos(\alpha - |\theta(t)|) - p^2 \operatorname{sgn}[\theta(t)] \sin(\alpha - |\theta(t)|), \quad (93)$$

where  $p^2 = 3g/(4R)$ . By substituting  $\alpha = \pi/2 - \beta_0$ , eqn. (93) can be rewritten as

$$\ddot{\theta}(t) = \ddot{\zeta}(t) \sin(|\theta(t)| + \beta_0) - p^2 \operatorname{sgn}[\theta(t)] \cos(|\theta(t)| + \beta_0), \quad (94)$$

which is similar to equation of motion (42) for the structural unit cell subject to a constant vertical load  $\bar{\mathcal{V}} = -p^2$  and  $\mathcal{C} = \mathcal{H}(\tau) = \ddot{\nu}(\tau) = 0$  and differs only in the time normalization and in the linear term in rotation due to the presence of the rotational spring.

Next, by considering the dissipation at impact through the velocity reduction factor  $e = \dot{\theta}(t_*^+)/\dot{\theta}(t_*^-) \in (0, 1)$ , the jump in the kinetic energy  $\mathcal{T}$  at the time of impact  $t_*$  follows as

$$\llbracket \mathcal{T}(t_*) \rrbracket = -\frac{2(1-e)MR^2}{3} \left\{ (1+e) \left[ \dot{\theta}(t_*^-) \right]^2 + 2\dot{\theta}(t_*^-)\dot{\zeta}(t_*) \cos \alpha \right\}. \quad (95)$$

This last equation shows that in the absence of ground motion ( $\dot{\zeta}(t_*) = 0$ ) the jump in the kinetic energy is always negative,  $\llbracket \mathcal{T}(t_*) \rrbracket < 0$ , since  $e < 1$ . However, in the presence of non-null ground velocity, a kinetic energy decrease is guaranteed only when the following conditions are both satisfied

$$\dot{\theta}(t_*^-)\dot{\zeta}(t_*) > 0, \quad \text{and} \quad |\dot{\zeta}(t_*)| < \frac{1+e}{2\cos \alpha} \left| \dot{\theta}(t_*^-) \right|. \quad (96)$$

Finally, from small vibrations analysis in the absence of ground motion, when an initial small rotation  $\theta_0$  is assumed together with a null initial velocity, the oscillation period for the system in the absence of impact dissipation ( $e = 1$ ) is approximated by

$$T_0(\theta_0) \approx 4\sqrt{\frac{2|\theta_0|}{p^2 \sin \alpha}}, \quad (97)$$

when  $\theta_0 \ll \alpha$ , while it is approximated by

$$T_0(\theta_0) \approx \frac{4}{p} \operatorname{arccosh} \left[ \frac{1}{1 - \frac{|\theta_0|}{\alpha}} \right], \quad (98)$$

when  $\theta_0 \approx \alpha$ , recalling the overturning initial rotation for the rocking problem  $|\theta_0| > \alpha$ . It is noted that, by considering impact dissipation through the velocity reduction factor  $e$ , the amplitude  $\theta_D^{\{n\}}$  and period  $T_D^{\{n\}}$  of the  $n$ -th cycle (each cycle encompassing two impacts) and the end time  $t_{\text{fin}}$  of rocking are approximated by the same expressions, eqns. (71)–(73), derived for the structural unit cell investigated in the main text.